Universidade Federal do Rio de Janeiro
Observatório do Valongo
Departamento de Astronomia

Projeto Final de Curso para a Obtenção do Título de Astrônomo

Variabilidade Espectral de Estrelas T Tauri: GQ Lupi

Aluno: Eduardo Seperuelo Duarte
Orientador: Flávio Pereira (ON/MCT)

Rio de Janeiro, Outubro de 2002.

À minha família.

Agradecimentos

Aos meus pais Célio e Norma e irmãos Ricardo e Leonardo, que sempre me apoiaram e incentivaram.

Aos meus avós, que me obrigavam a me manter atualizado fazendo perguntas à respeito dos astros.

Aos meus orientadores, Celso Batalha, Flávio Pereira e Dalton Lopes, pela confiança e oportunidade que me ofereceram.

À todos os professores do Valongo e do Fundão, que sem dúvida contribuíram muito para minha formação.

E é claro, aos meus amigos, que não citarei os nomes pois, felizmente, são muitos.

Grande parte do meu trabalho de iniciação científica, como bolsista do PIBIC, e que resultou nesta monografia, foi realizada sob a orientação de Celso Batalha.

Resumo

Apresentamos a série temporal de observações de baixa resolução da estrela GQ Lupi, uma estrela T Tauri que apresenta fortes indícios de um disco de acresção circunstelar. Nosso conjunto de dados consiste em 18 observações realizadas durante 18 noites consecutivas no mês de Fevereiro de 1999. Medimos a distribuição do excesso de contínuo (velamento) e determinamos o velamento médio para cada noite de observação. A série temporal do velamento apresentou um comportamento senoidal com um período de aproximadamente 13 dias. Acreditamos que uma mancha quente na superfície estelar que rotaciona junto com a estrela é a responsável por esse comportamento do velamento. A Fotometria da Gq Lupi encontrada na literatura e nossas observações espectrofotométricas de 1998 confirmam este período encontrado para o velamento. A série temporal do velamento não apresentou uma boa correlação com as linhas de emissão. Porém, correlações entre as linhas de emissão indicam uma região comum de formação ou um mecanismo físico governando suas luminosidades ao mesmo tempo. Os perfis P Cygni invertido praticamente desapareceram em relação aos dados de 1998.

As observações foram realizadas no European Southern Observatory, La Silla, Chile sob o acordo ESO-ON.

Palavras-chave: acresção, discos de acresção; estrelas: individual (GQ Lupi); estrelas: pré-sequência principal

Abstract

We present the 1999 low resolution time series of GQ Lupi, a typical T Tauri star with strong evidence of circumstelar disk accretion. Our unique data set consist of 18 exposures taken during 18 consecutive nights in February 1999. We compute the excess continuum emission distribution (veiling) and determine the average veiling. The resulting veiling time series has a sinusoidal curve that shows a displacement between minima of about 13 days. We argue that this bell shaped curve is controlled by an accretion hot spot, on the stellar surface, crossing the line of sight as the star rotates. Further support for this period is found in previously published photometry of GQ Lupi as well as in our 1998 spectrophotometric campaign. The veiling time series does not have a good correlation with the emission lines. On the contrary, individual line emission correlate with one another indicating the presence of a common mechanism governing their luminosities or a commom formation region. The inverse P Cygni profiles that are so conspicuously present in the Balmer lines and in the CaII H and K lines practically disappear in the present data set. The observations were taken on the European Southern Observatory, La Silla, Chile, under the ESO-Observatório Nacional agreement.

Subject headings: accretion, accretion disks; stars: individual (GQ Lupi); stars: pre main sequence

Conteúdo

Dedicatória 1
Agradecimentos 2
Resumo 3
Abstract 4
Índice 5
Lista de Figuras 6
Lista de Tabelas 7

1 Introdução **8**

2 Observações **12**
2.1 Instrumentação, Redução de Dados e Calibração de Fluxos 12

3 Velamento **16**

4 As Linhas de Emissão **21**

5 Conclusões e Perspectivas Futuras **28**
5.1 Análise de Periodograma 28
5.2 Correlações 29
5.3 Perspectivas Futuras 30

Bibliografia **31**

A Artigo - Variability of Southern T Tauri Stars (VAST) III: The Continnum Flux Changes of The TW Hya Bright Spot) **34**

Lista de Figuras

1.1 Posições no diagrama HR de estrelas jovens da nuvem molecular de Taurus-Auriga. WTTS são as estrelas T Tauri Fracas, CTTS são estrelas T Tauri Clássicas e ZAMS é a sigla em inglês para seqüência principal de idade zero. 9

2.1 Observações espectrofotométricas da GQ Lupi do mês de Fevereiro de 1999. 13
2.2 Observações espectrofotométricas da GQ Lupi do mês de Fevereiro de 1999. 14
2.3 Observações espectrofotométricas da GQ Lupi do mês de Fevereiro de 1999. As linhas de emissão estiveram presentes em todas as noites. 14

3.1 A figura acima mostra como funciona o método utilizado para a determinação do velamento. O espectro da padrão é apresentado em linha-losângulo. 17
3.2 O espectro da padrão foi velado até que o fundo de sua linha coincidisse com o da T Tauri. A linha selecionada para a determinação do velamento nesse exemplo é a linha do CaII em 4226 Å. 17
3.3 Distribuição espectral do velamento da noite 1 até a noite 6, obtida utilizando o método descrito acima. 18
3.4 Distribuição espectral do velamento da noite 7 até a noite 12. 19
3.5 Distribuição espectral do velamento da noite 13 até a noite 18. 19

4.1 Correlação entre as linhas de emissão e o velamento. 24
4.2 Correlação entre as linhas de emissão. 25
4.3 Correlação entre Hγ e linhas de elementos diferentes. 25
4.4 Correlação entre as linhas do HeI e CaII. 26

5.1 Variabilidade do velamento médio. 29

Capítulo 1

Introdução

As estrelas jovens de baixa massa ($\leq 2M_{\odot}$) foram originalmente propostas como sendo um subconjunto dos objetos que apresentavam linhas de emissão, especialmente a linha Balmer α do hidrogênio (Hα) em 6563 Å = 0.6563 μm. A juventude dessas estrelas foi sugerida devido as suas correlações espaciais com nebulosas de reflexão e nuvens escuras (Joy, 1945) e devido ao fato de estarem relativamente próximas de associações de estrelas de alta massa (O-B) que são necessariamente jovens. Este subconjunto é agora entendido como sendo o resultado da formação de estrelas em nuvens moleculares; estrelas com idades $\leq 10^6$ anos não podem viajar para regiões distantes dos seus locais de formação dada as baixas velocidades de dispersão ($\leq$ 1-2 km s^{-1}) relativas ao gás molecular.

Um levantamento de estrelas com linhas de emissão intensas gerou o primeiro catálogo extensivo de estrelas jovens (Herbig & Bell, 1988). Com o advento de técnicas no infravermelho, foram encontrados vários outros objetos até então fortemente obscurecidos no óptico pela poeira presente nas regiões circunstelares. Alguns dos mais densos aglomerados conhecidos de estrelas recém formadas foram somente detectados quando imagens dos complexos de nuvens moleculares foram geradas por observações no infravermelho (Lada *et al.* 1991). Apesar da forte extinção do material circunstelar remanescente, a emissão de raio-X também tem sido utilizada para identificar mais objetos jovens, especialmente estrelas que não apresentam forte excesso de emissão no infravermelho ou no óptico.

Várias estrelas de baixa massa associadas com nuvens moleculares localizam-se acima da seqüência principal no diagrama HR (Figura 1.1). Suas baixas massas M_* e seus raios R_* característicos de estrelas giantes ou subgigantes, indicam temperaturas centrais muito baixas para fundir o hidrogênio em hélio, uma vez que as temperaturas internas são proporcionais à M_*/R_*. A fusão do deutério ocorre a temperaturas mais baixas do que a fusão do hidrogênio, mas como a abundância de deutério é relativamente baixa, as luminosidades

das estrelas jovens são parcialmente providas pela queima do deutério por somente alguns milhões de anos. Sem a liberação da energia de fusão, a estrela jovem deve se contrair, gerando energia potencial gravitacional para repor a energia perdida pela radiação da fotosfera estelar. Esta contração corresponde a mover-se para baixo no diagrama HR (Figura 1.1), e portanto, as posições das estrelas jovens no diagrama HR podem ser usadas para estimar idades. Esta contração é interrompida quando a liberação da energia de fusão do hidrogênio equilibra a energia irradiada pela fotosfera estelar. Na verdade, as idades das estrelas próximas a "seqüência principal de idade zero" (SPIZ) são difíceis de serem determinadas, especialmente quando as incertezas nas luminosidades estelares, devido aos erros relacionados com a distância e a extinção causada pela poeira, são levadas em conta.

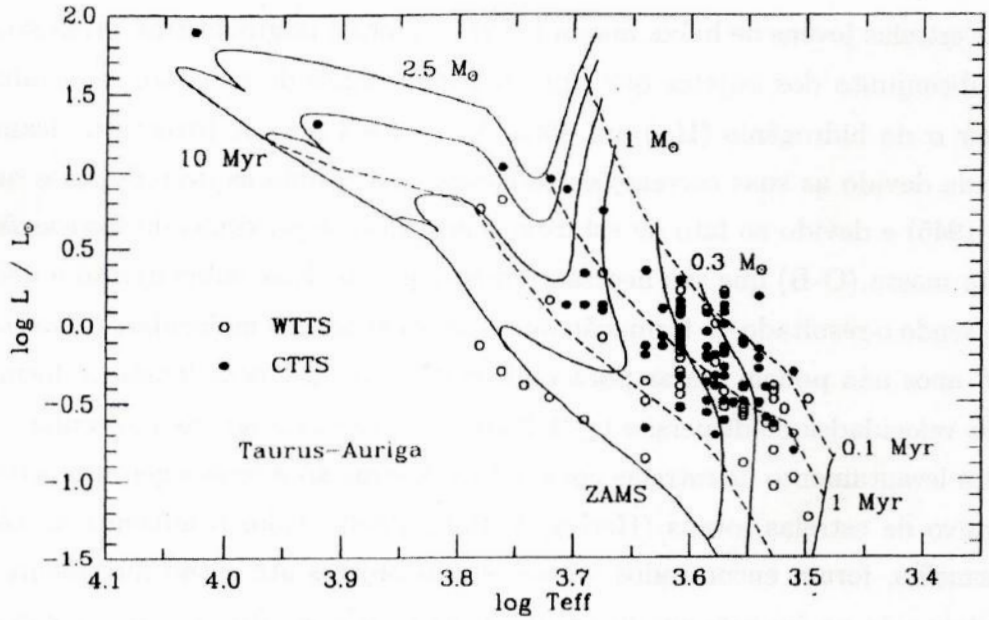

FIGURA 1.1: Posições no diagrama HR de estrelas jovens da nuvem molecular de Taurus-Auriga. WTTS são as estrelas T Tauri Fracas, CTTS são estrelas T Tauri Clássicas e ZAMS é a sigla em inglês para seqüência principal de idade zero.

As estrelas pré-seqüência principal de baixa massa ($M \leq 2M_{\odot}$), que possuem tipos espectrais F-M (correspondendo a temperaturas efetivas superficiais $\sim$ 7000 K - 3000 K), são chamadas estrelas "T Tauri" (Joy, 1945h; Bertout, 1989); estrelas pré-seqüência principal de massas maiores (entre 2 e 10 $M_{\odot}$) são denominadas estrelas "Herbig Ae/Be" (Herbig, 1960) para distinguí-las de outros tipos de estrelas com linhas de emissão e tipos espectrais A-B (temperaturas efetivas 8000-30000K) que são presumidamente mais evoluídas. (Os intervalos de massa não são exatos uma vez que a classificação depende do tipo espectral

estelar ou da temperatura efetiva, no qual podem variar substancialmente. A rapidez com que estrelas massivas evoluem torna os estudos de evolução estelar mais difíceis. Estrelas com massas $\geq 2M_{\odot}$ são geralmente encontradas próximas a SPIZ (Figura 1.1); as idades estimadas para esses objetos são incertas.

As estrelas T Tauri foram originalmente identificadas como estrelas de tipo tardio com intensas linhas de emissão e variações irregulares de luz associadas a nebulosas escuras ou brilhantes (Bertout, 1989). Desde então, o termo " estrela T Tauri " tornou-se sinônimo de estrelas pré-seqüência principal de baixa massa, tendo ou não, associação com nebulosas ou intensas linhas de emissão. A maioria das estrelas variáveis inicialmente identificadas como estrelas T Tauri são atualmente chamadas de estrelas T Tauri "clássica" (ETTC) ou "de emissão forte", para distinguí-las das estrelas T Tauri "de emissão fraca" (ETTF). A distinção entre emissão forte e fraca é geralmente realizada com base na emissão de Hα: se a largura equivalente de Hα é menor que 10Å, o objeto é classificado como ETTF (Catálogo de Herbig & Bell, 1988). Apesar desta classificação ser muito utilizada para estrelas K-M, ela pode não funcionar quando aplicada as estrelas mais quentes F-G, uma vez que o campo de radiação fotosférico dessas estrelas tende a encobrir a emissão de Hα. Aparentemente o excesso de emissão de várias ETTF pode ser explicado em termos da intensa atividade magnética, enquanto que os níveis extremos de excesso de emissão no óptico e no infravermelho de várias ETTC, requerem uma fonte de energia externa.

Provavelmente, a acresção de matéria de um disco circunstelar é a responsável pelo excesso de emissão das ETTC (Lynden-Bell & Pringle, 1974). A queda de matéria na estrela central produz a emissão de contínuo de alta temperatura no óptico e no ultravioleta além de intensas linhas de emissão no óptico. Essa emissão de contínuo, é a responsável pelo fenômeno conhecido como velamento, que será considerado com mais detalhes nos capítulos subseqüentes.

Em alguns casos o excesso de emissão de contínuo no óptico e no ultravioleta excede a emissão da fotosfera estelar. Isto acontece para aproximadamente 5-10% das estrelas T Tauris mais bem estudadas na região da nuvem molecular de Taurus (Kenyon & Hartmann, 1995). Nestes objetos, a energia de acresção liberada é a fonte de luminosidade dominante no sistema. Nossa compreensão com relação aos estados de evolução das ETTC ainda é fraca, devido às intensas emissões de contínuo nos comprimentos de ondas do óptico, tornando muito difícil determinar posições confiáveis destas estrelas no diagrama HR.

Originalmente, acreditava-se que a emissão de alta temperatura era produzida na camada limite entre o disco e a estrela, devido às suas velocidades de rotação serem diferentes (Lynden-Bell & Pringle, 1974). Agora, parece mais provável que o disco interno é rompido pelo campo magnético da estrela T Tauri central; isto resulta numa acresção magnética, no

qual o material do disco é canalizado ao longo das linhas do campo magnético até colidir na estrela (Konigl, 1991; Camenzind, 1990). Acredita-se que a emissão de contínuo surge do choque na base da coluna de acresção magnética, próximo à superfície estelar, enquanto que as linhas de emissão surgem do gás, movendo-se em queda livre, no funil magnético, no qual é aquecido até temperaturas de $\sim$ 8000K (Calvet & Hartmann, 1992; Hartmann, Hewett, & Calvet, 1994). Os perfis das linhas de emissão no óptico produzidos por esta queda do gás exibem assimetrias, como a absorção deslocada para o vermelho (Hartmann *et al.* 1994). Estrelas T Tauri que apresentam perfis de linhas assimétricos foram inicialmente chamadas de estrelas YY Ori. Estudos mais recentes utilizando espectros de alta resolução, mostram que assimetrias do tipo YY Ori são comuns em ETTC, indicando que a maioria das estrelas T Tauri ganham material do disco através de suas magnetosferas (Edwards *et al.* 1994).

Neste trabalho apresentamos medidas do excesso de contínuo (velamento), das larguras equivalentes das linhas de emissão, e a variabilidade destes parâmetros ao longo de 18 noites de observação da estrela T Tauri GQ Lupi, uma representante da subclasse YY Ori. O capítulo 2 versa sobre as observações, onde descrevemos os instrumentos e procedimentos utilizados na obtenção e redução dos dados. No capítulo 3, definimos o velamento e descrevemos o método utilizado para determiná-lo. O capítulo 4 está dedicado ao estudo das linhas de emissão e suas correlações. Finalmente, discutimos no capítulo 5 as conclusões e mostramos as perspectivas futuras de nosso trabalho.

Capítulo 2

Observações

Os dados apresentados neste trabalho foram observados durante 18 noites consecutivas no mês de Fevereiro de 1999. Os principais motivos da escolha da GQ Lupi, uma estrela K7 V (Herbig & Bell, 1988), como principal alvo de nossas observações foram o comportamento dos perfis P Cygni invertido (PCI) presentes nas linhas de Balmer de ordem superiores a Hβ e nas linhas H & K do CaII e a variabilidade regular do excesso de contínuo (velamento) (Batalha, Lopes, & Batalha, 2001, BLB). Ao contrário do que foi relatado em BLB, em nossas observações praticamente não há mais a presença do PCI e o velamento continuou apresentando um comportamento bastante regular.

2.1 Instrumentação, Redução de Dados e Calibração de Fluxos

Observações espectrofotométricas foram coletadas em La Silla com o telescópio de 1,52m do ESO e com o espectrógrafo Boller & Chivens. As janelas espectrais estendem-se de 4200 Å à 6200 Å e 3500 Å à 7200 Å (ver Figuras 2.1 a 2.3). Foram escolhidas as redes de difração no. 31 e 33. Para obter uma razão sinal/ruído maior que 100 para uma estrela com magnitude V = 12, o tempo de integração variou entre 10 à 15 minutos. Utilizamos um CCD Loral Lesser (2048 x 2048), fornecendo uma resolução de 2 Å na janela de 4200 Å a 6200 Å e 4 Å na janela de 3500 Å a 7200 Å. Os dados foram reduzidos seguindo o procedimento padrão: subtração do bias, flat-fielding e extração das diferentes ordens Echelle seguindo-se uma prescrição adotada por Jeff Valenti (1994) e descrita em sua tese de doutorado. O espectro encontra-se portanto reduzido em unidades relativas de fluxo, fazendo-se neccessário convertê-lo para unidades de fluxo absolutas (erg cm^{-2} s^{-1} $Å^{-1}$) tendo em vista os objetivos do projeto. Assim, observamos nossos objetos com uma fenda

de 5 arcsec dada a necessidade de evitarmos perdas de luz. Da mesma forma, procuramos fazer a correção paralática evitando perdas diferenciadas em comprimento de onda devido à refração atmosférica. Estas correções foram realizadas posicionando-se a fenda relativa à estrela alvo com ângulos fornecidos por Filippenko (1982). Observamos duas estrelas padrões espectrofotométricas (Hiltner 600 e CD 32-9927), ao longo das 18 noites, com a finalidade de convertermos os dados reduzidos em unidades relativas de fluxo para unidades absolutas de fluxo.

Para realizar essa conversão, fizemos a correção da extinção atmosférica pela expressão $F = F_0\ 10^{\theta k}$ onde θ é a massa de ar e k o coeficiente de extinção atmosférico de La Silla (1999), fornecido pelo Grupo de Fotometria do Observatório de Gênova.

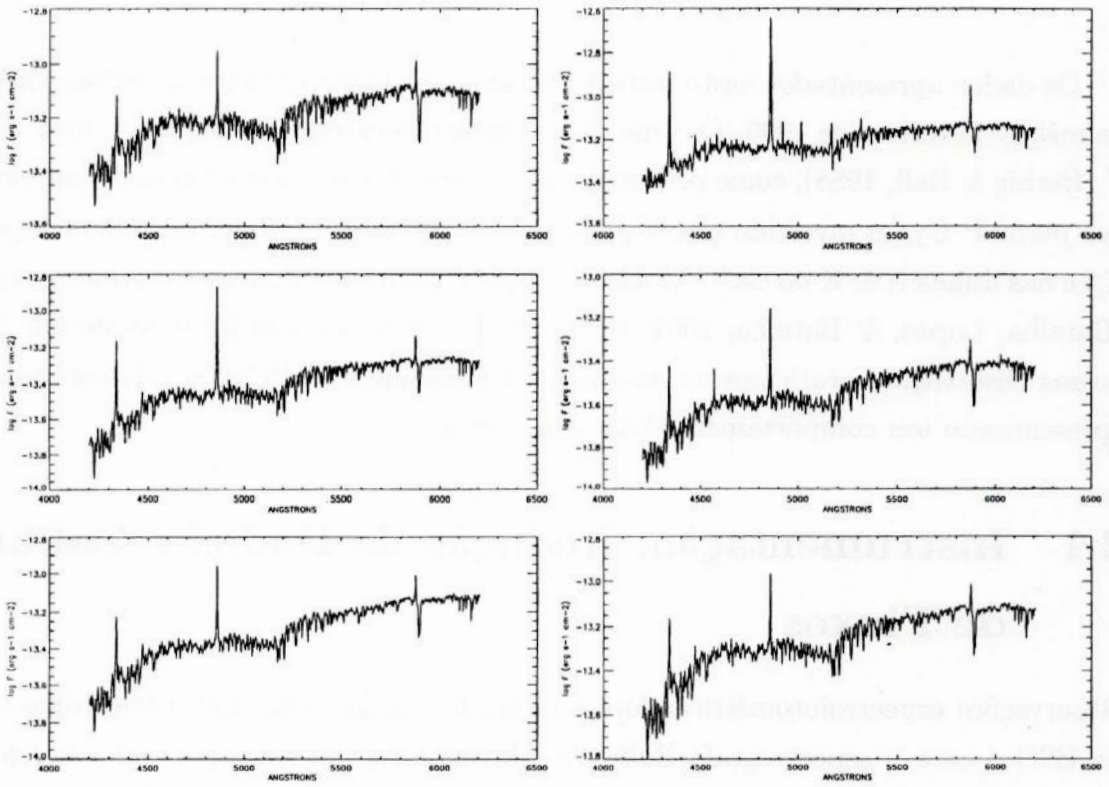

FIGURA 2.1: Observações espectrofotométricas da GQ Lupi do mês de Fevereiro de 1999.

Mostramos, nas figuras 2.1-3, as características espectrofotométricas da estrela GQ Lupi obtidas durante as 18 noites de observação. É interessante notar a presença das linhas de emissão e suas variabilidades ao longo das noites de observação. O P Cygni invertido, presente um ano antes principalmente na linha Hβ (BLB), desapareceu em nossas observações. A partir da 12ª noite (Figura 2.2, último gráfico), o intervalo espectral aumentou para 3500 Å à 7200 Å, cobrindo toda a região da série de Balmer.

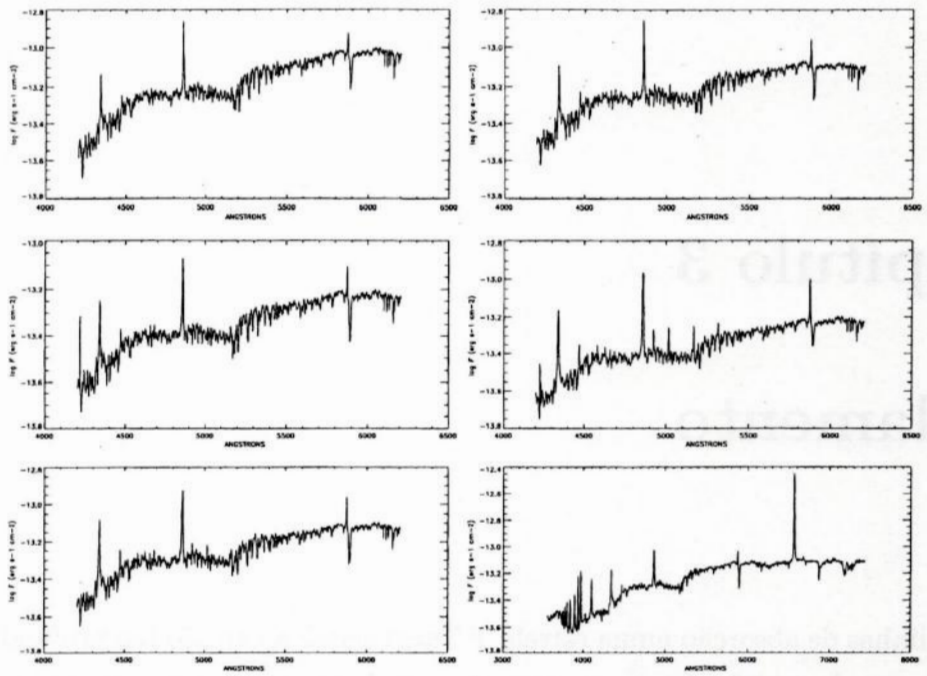

FIGURA 2.2: Observações espectrofotométricas da GQ Lupi do mês de Fevereiro de 1999.

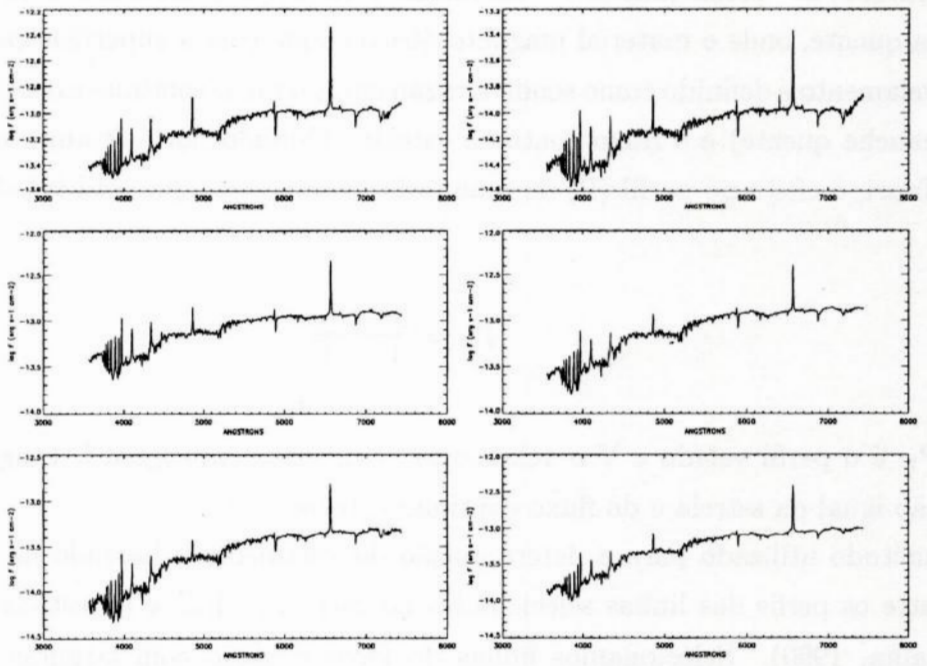

FIGURA 2.3: Observações espectrofotométricas da GQ Lupi do mês de Fevereiro de 1999. As linhas de emissão estiveram presentes em todas as noites.

Capítulo 3

Velamento

As linhas de absorção numa estrela T Tauri clássica não são tão profundas como aquelas de uma estrela padrão de mesmo tipo espectral. O espectro da estrela jovem parece estar "velado" por uma emissão externa de contínuo. Este efeito é chamado de velamento e estende-se para o ultravioleta sendo uma importante fonte de energia. O velamento tem sido atribuído ao "preenchimento" das linhas de absorção fotosféricas pela emissão de uma mancha quente, onde o material magnetosférico colide com a superfície estelar.

O velamento é definido como sendo a razão entre o fluxo contínuo externo (fluxo emitido pela mancha quente) e o fluxo contínuo estelar. Quando normalizamos o fluxo contínuo da T Tauri, o efeito no perfil (P) de uma linha de absorção que está velada é

$$P_V = \frac{P + V}{1 + V}$$

onde P_V é o perfil velado e V o velamento. Um velamento igual à 1 significa uma contribuição igual da estrela e do fluxo contínuo externo.

O método utilizado para a determinação do velamento é baseado na comparação direta entre os perfis das linhas selecionadas na estrela padrão e na estrela T Tauri (Basri & Batalha, 1990). Selecionamos linhas do ferro e cálcio com larguras equivalentes de aproximadamente 100 mÅ do espectro solar (Moore, Minnaert, & Houtgast, 1966).

O contínuo da estrela padrão, assim como o contínuo da estrela T Tauri, é normalizado em intervalos de 150 Å. O velamento obtido para uma determinada linha é aquele que ajusta a profundidade da linha da padrão à profundidade da linha da estrela T Tauri. As figuras 3.1 e 3.2 mostram como o método funciona utilizando a linha do CaII em 4226 Å.

Para determinar o velamento da GQ Lupi, utilizamos a distribuição espectral de uma

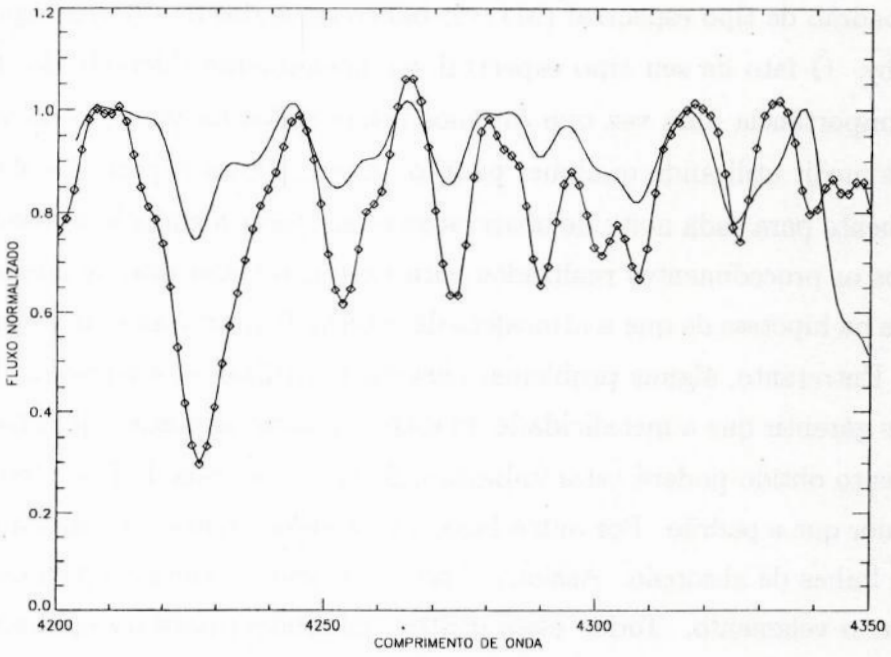

FIGURA 3.1: A figura acima mostra como funciona o método utilizado para a determinação do velamento. O espectro da padrão é apresentado em linha-losângulo.

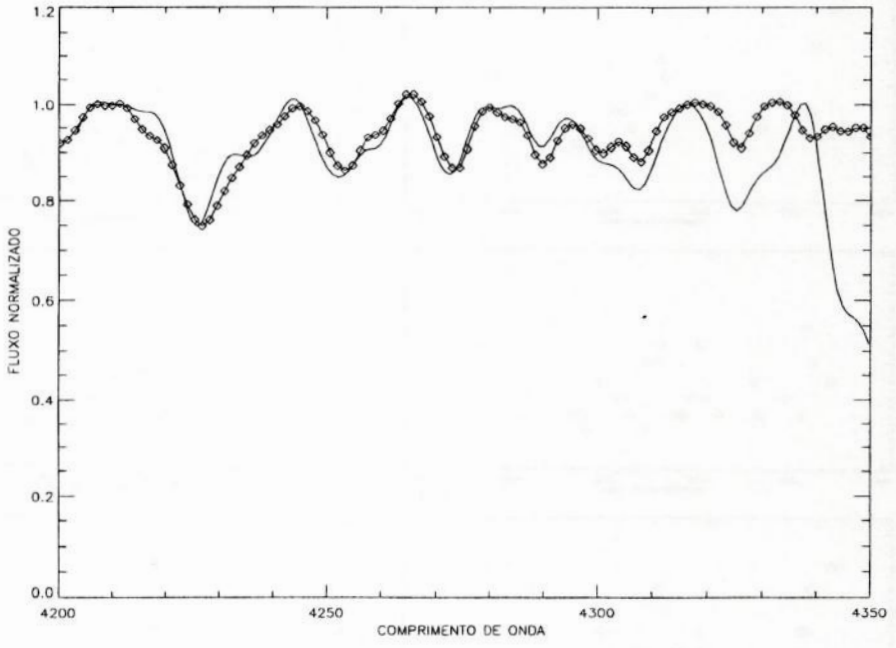

FIGURA 3.2: O espectro da padrão foi velado até que o fundo de sua linha coincidisse com o da T Tauri. A linha selecionada para a determinação do velamento nesse exemplo é a linha do CaII em 4226 Å.

estrela padrão de tipo espectral (M1) do banco de dados de estrelas espectrofotométricas de Jacoby. O fato de seu tipo espectral ser ligeiramente diferente da T Tauri não é de grande importância uma vez que estamos interessados na variação do velamento, a qual podemos medir utilizando qualquer padrão. Assim, fomos capazes de obter a distribuição de velamento para cada noite de observação e recuperar a emissão fotosférica da GQ Lupi.

Todos os procedimentos realizados para extrair o velamento de nossos espectros estão baseados na hipótese de que a atmosfera da estrela T Tauri é similar à atmosfera da estrela padrão. Entretanto, alguns problemas surgem ao utilizar esta hipótese. Uma vez que não podemos garantir que a metalicidade da estrela padrão adotada seja a mesma da T Tauri, o velamento obtido poderá estar subestimado caso a estrela T Tauri tenha uma metalicidade maior que a padrão. Por outro lado, a cromosfera tende a reduzir a profundidade das intensas linhas de absorção. Assim, o "preenchimento" causado pela cromosfera tende a aumentar o velamento. Todos esses efeitos contribuem para o espalhamento encontrado em nossas medidas. Estimamos que as incertezas nas medidas de velamento são de aproximadamente 0,1. Nas figuras 3.3, 3.4 e 3.5 apresentamos a distribuição de velamento para cada uma das noites de observação.

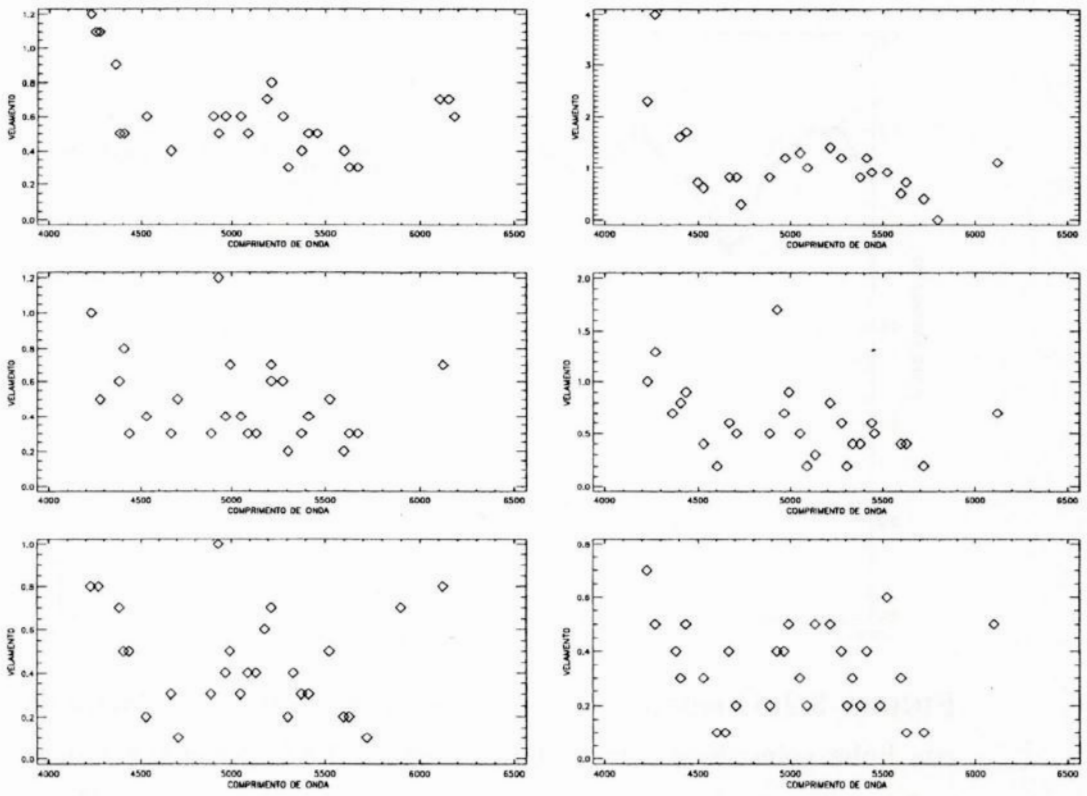

FIGURA 3.3: Distribuição espectral do velamento da noite 1 até a noite 6, obtida utilizando o método descrito acima.

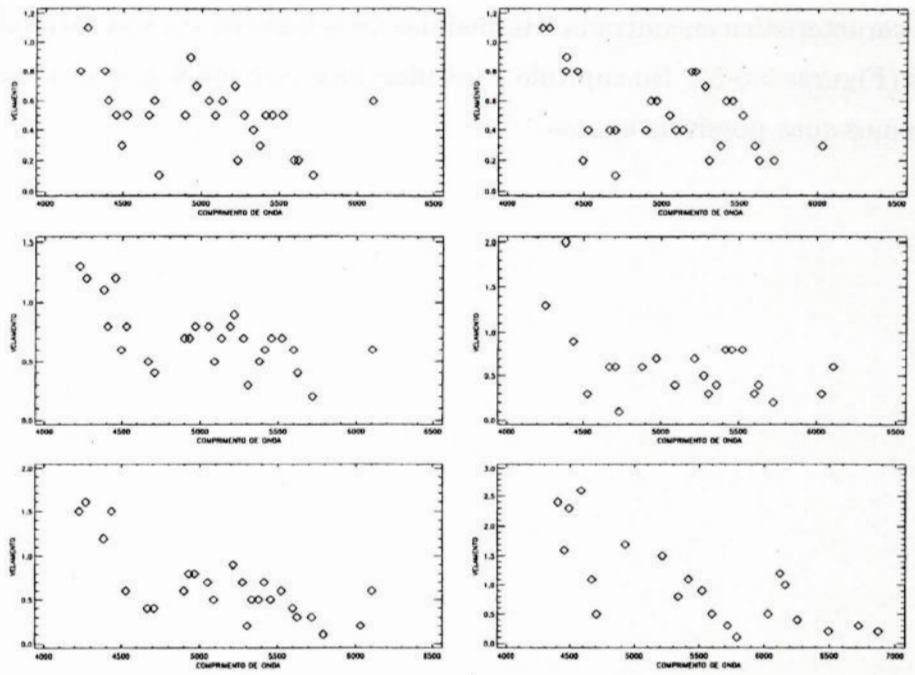

FIGURA 3.4: Distribuição espectral do velamento da noite 7 até a noite 12.

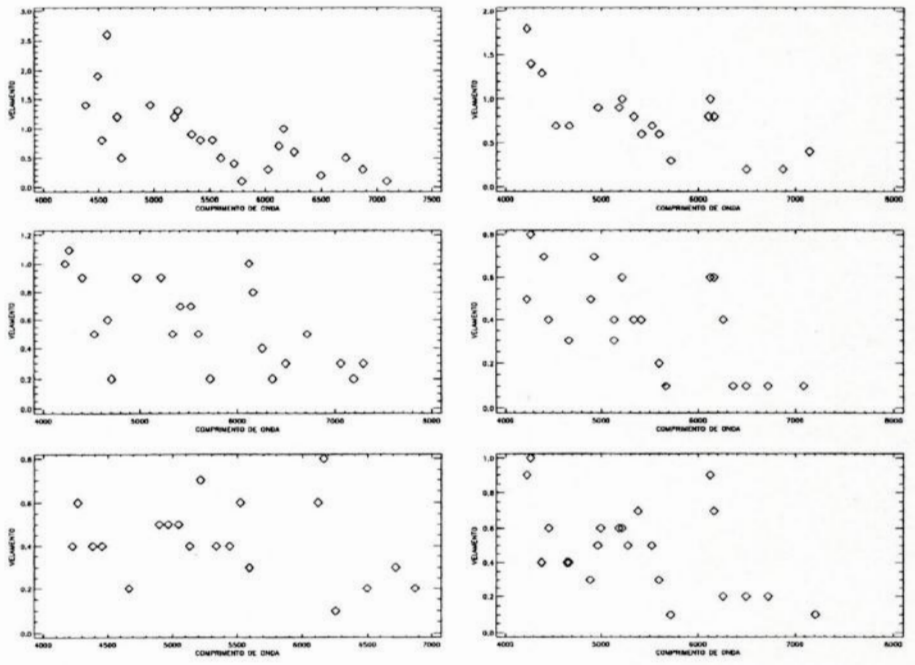

FIGURA 3.5: Distribuição espectral do velamento da noite 13 até a noite 18.

Observamos, nas figuras 3.3-5, o comportamento do velamento em relação ao comprimento de onda. O velamento é maior para comprimentos de onda menores. Isso se deve ao fato da temperaura da mancha quente, que está produzindo o excesso de contínuo, ser maior que a temperatura da fotosfera da T Tauri.

Outra característica encontrada nas medidas de velamento é a sua variabilidade ao longo das noites (Figuras 3.3-5). No capítulo 5 estudaremos com mais detalhes essa variabilidade e discutiremos suas possíveis causas.

Capítulo 4

As Linhas de Emissão

Neste capítulo, nos concentraremos nas intensas linhas de emissão que aparecem em todas as nossas observações da estrela GQ Lupi. São elas: série de Balmer do Hidrogênio, as linhas H & K do CaII, e linhas do HeI (5876Å e 4462Å). As medidas de fluxo e largura equivalente estão apresentadas nas tabelas 4.1 e 4.2.

O estudo das correlações entre os fluxos de diferentes linhas é uma importante ferramenta que fornece uma melhor compreensão das relações entre as diferentes regiões formadoras de linhas. As correlações podem indicar que as linhas são formadas numa região comum ou que um determinado processo físico está afetando regiões diferentes ao mesmo tempo.

Inicialmente medimos o fluxo integrado (ergs s^{-1} cm^{-2}) das linhas de emissão e comparamos com as medidas de velamento. Estimamos incertezas menores que 9% em nossas medidas de fluxo. A figura 4.1 mostra o fluxo integrado das linhas HeI (5876 Å), Hβ, HeI (4462 Å) e Hγ em função do velamento médio de cada noite (a média de todas as medidas de velamento sobre o intevalo espectral).

Das quatro linhas apresentadas na Figura 4.1, apenas a linha do HeI (5876 Å) não apresentou uma boa correlação com o velamento. O grau das correlações pode ser medido calculando o coeficiente de correlação linear de Pearson e sua probabilidade de alarme falso (PAF), que mede a probabilidade de uma aparente correlação ocorrer ao acaso (Bevington, 1969). A PAF depende do coeficiente de correlação linear e do número de pontos usado na correlação. Uma boa correlação terá um coeficiente de correlação linear próximo a 1 e uma baixa PAF. A PAF das linhas HeI (5876 Å), Hβ, HeI (4462 Å) e Hγ correlacionadas com o velamento como mostra a Figura 4.1 foi: 0,3813, 0,0608, 0,0990 e 0,0471 respectivamente. As demais linhas não apresentaram correlação com o velamento.

TABELA 4.1: Medidas de Fluxo x 10^{-13} (ergs s^{-1} cm^{-2}) e Largura Equivalente das Linhas de Emissão

Data Juliana	F(Hα)	W(Hα)	F(HeI) (5876Å)	W(HeI) (5876Å)	F(Hβ)	W(Hβ)	F(HeI) (4462Å)	W(HeI) (4462Å)	F(Hγ)	W(Hγ)	F(Hδ)	W(Hδ)	F(CaII) (H)	W(CaII) (H)
2451218.8851			0,6	0,8	2,4	3,6	0,1	0,3	1,7	3,4				
2451219.8488			1,7	2,5	10,8	18,2	0,4	0,7	5,2	11,1				
2451220.8447			0,7	1,4	5,4	15,0	0,1	0,5	2,5	10,0				
2451221.8439			0,5	1,2	2,0	7,3	0,07	0,3	1,1	6,0				
2451222.8750			1,1	1,4	3,2	7,0	0,2	0,5	1,6	5,6				
2451223.8677			0,9	1,2	2,3	4,4	0,1	0,3	1,5	4,2				
2451224.8567			1,0	1,0	4,0	6,5	0,1	0,3	2,1	5,2				
2451225.8527			0,8	0,9	4,4	7,3	0,3	0,5	2,6	6,1				
2451226.8395			0,6	1,0	3,2	7,7	0,2	0,5	1,7	5,4				
2451227.8568			1,8	2,8	5,8	14,2	0,5	1,4	3,6	12,3				
2451228.8348			1,3	1,7	5,6	10,8	0,3	0,7	3,1	7,8				
2451229.8288	30,9	37,8	0,8	1,1	4,8	9,1	0,3	0,6	3,2	8,2	2,8	8,8	3,4	12,4
2451230.8552	39,5	35,3	1,2	1,1	6,3	8,9	0,5	0,7	4,0	7,5	3,9	9,1	4,2	11,1
2451231.8637	3,5	30,2	0,1	1,1	0,7	9,7	0,04	0,6	0,5	9,1	0,4	10,3	0,6	16,2
2451232.8679	35,3	28,6	1,3	1,1	6,1	8,2	0,5	0,8	4,9	9,7	4,9	12,8	6,9	22,6
2451233.8714	27,9	21,2	0,9	0,8	3,1	4,3	0,3	0,5	2,1	4,4	3,0	9,2	4,0	17,1
2451234.8676	11,1	23,3	0,3	0,6	1,2	5,2	0,03	0,2	0,9	5,8	1,0	9,9	1,5	21,1
2451235.8782	31,0	31,9	0,5	0,5	3,4	7,4	0,08	0,2	1,7	5,7	1,6	7,9	2,5	17,5

TABELA 4.2: Medidas de Fluxo x 10^{-13} (ergs s^{-1} cm^{-2} $Å^{-1}$) e Largura Equivalente das Linhas de Emissão

Data Juliana	F(CaII) (K)	W(CaII) (K)	F(H8)	W(H8)	F(H9)	W(H9)	F(H10)	W(H10)	F(H11)	W(H11)	F(H12)	W(H12)	F(H13)	W(H13)
2451218.8851														
2451219.8488														
2451220.8447														
2451221.8439														
2451222.8750														
2451223.8677														
2451224.8567														
2451225.8527														
2451226.8395														
2451227.8568														
2451228.8348														
2451229.8288	3,0	12,5	1,9	7,8	1,5	6,1	1,1	4,1	0,8	3,2	0,5	2,1	0,4	1,5
2451230.8552	2,6	7,5	2,7	8,1	2,2	6,4	1,6	4,7	1,1	3,1	0,8	2,4	0,5	1,5
2451231.8637	0,2	7,2	0,3	10,3	0,3	10,6	0,3	8,8	0,2	5,8	0,1	2,8	0,1	2,8
2451232.8679	3,0	12,3	4,0	15,3	3,7	14,8	2,8	10,3	2,2	7,4	1,3	4,1	0,8	2,5
2451233.8714	1,9	11,0	2,2	11,8	2,1	11,9	1,8	9,9	1,3	6,0	0,8	3,8	0,5	2,6
2451234.8676	0,8	15,7	0,7	12,6	0,7	12,3	0,7	12,1	0,5	7,9	0,3	5,2	0,1	2,3
2451235.8782	1,6	14,3	1,1	10,4	1,1	10,6	0,9	7,5	0,6	4,8	0,4	3,5	0,2	2,0

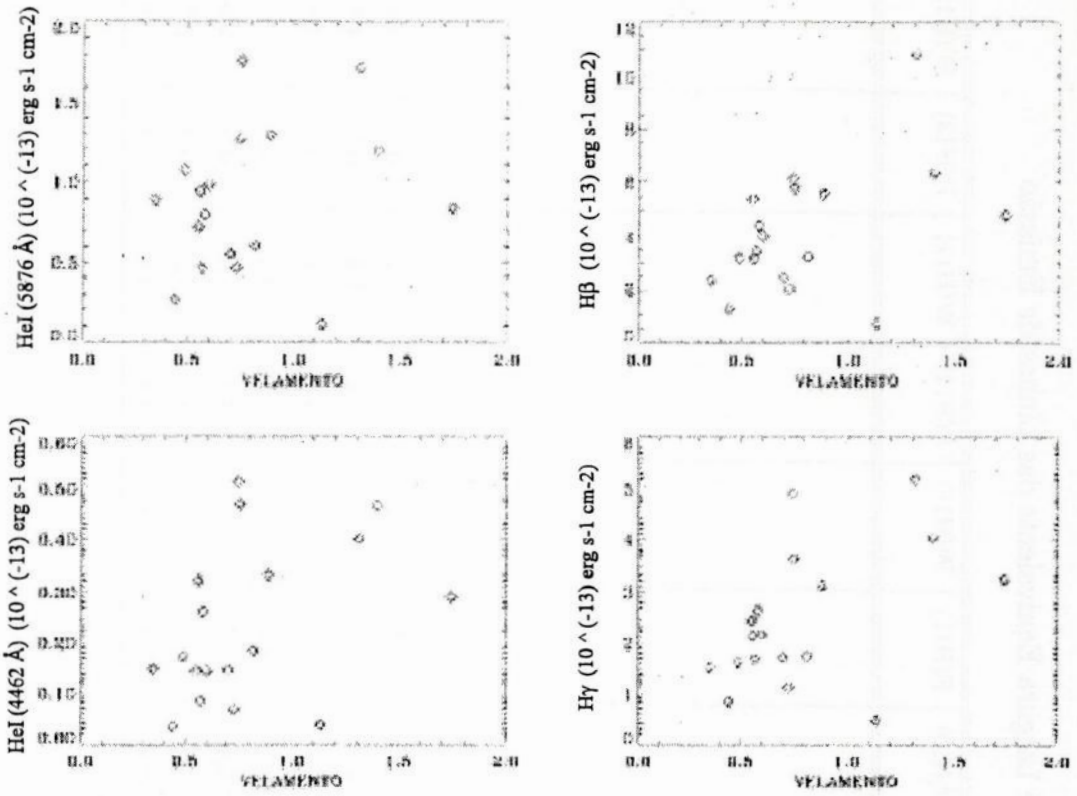

FIGURA 4.1: Correlação entre as linhas de emissão e o velamento.

As figuras 4.2 a 4.4 mostram correlações entre os fluxos integrados de diferentes linhas de emissão. Novamente, podemos medir o grau das correlações calculando a PAF para cada correlação (Tabela 4.3). Todas as linhas se correlacionam umas com as outras. A Figura 4.2 mostra as correlações entre linhas de mesma espécie: Hβ x Hγ, Hα x Hβ, HeI (5876 Å) x HeI (4462 Å) e CaII (H) x CaII (K).

Como era de se esperar, linhas de mesma espécie correlacionam-se entre si. As figuras 4.3 e 4.4, mostram as correlações de espécies diferentes.

Na figura 4.3 temos as correlações de Hγ com: HeI (5876 Å), HeI (4462 Å), CaII (H) e CaII (K). E na figura 4.4 temos: HeI (5876 Å) x CaII (H), HeI (5876 Å) x CaII (K), HeI (4462 Å) x CaII (H) e HeI (4462 Å) x CaII (K).

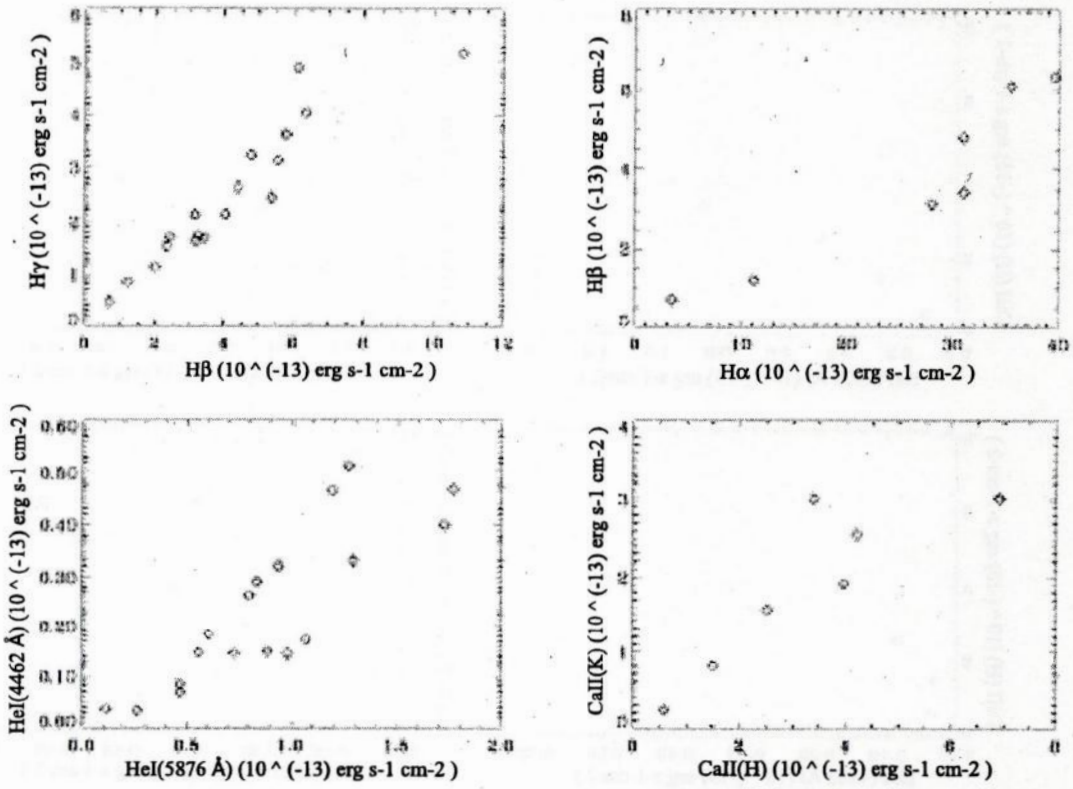

FIGURA 4.2: Correlação entre as linhas de emissão.

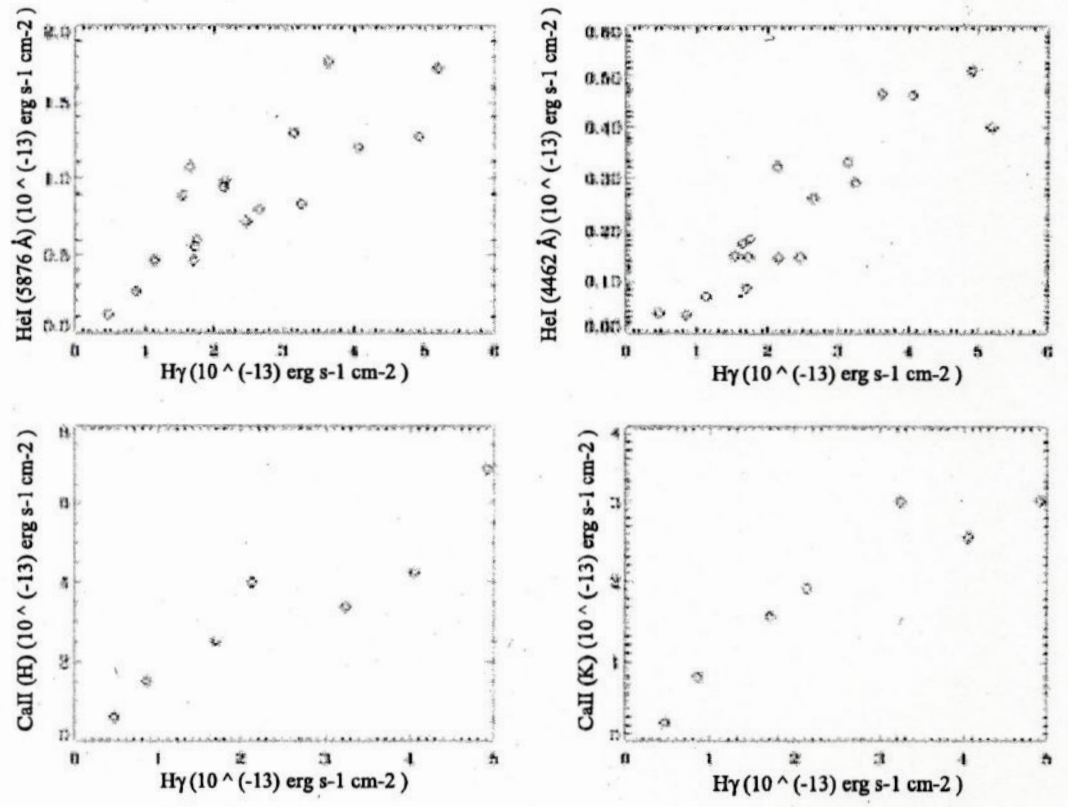

FIGURA 4.3: Correlação entre Hγ e linhas de elementos diferentes.

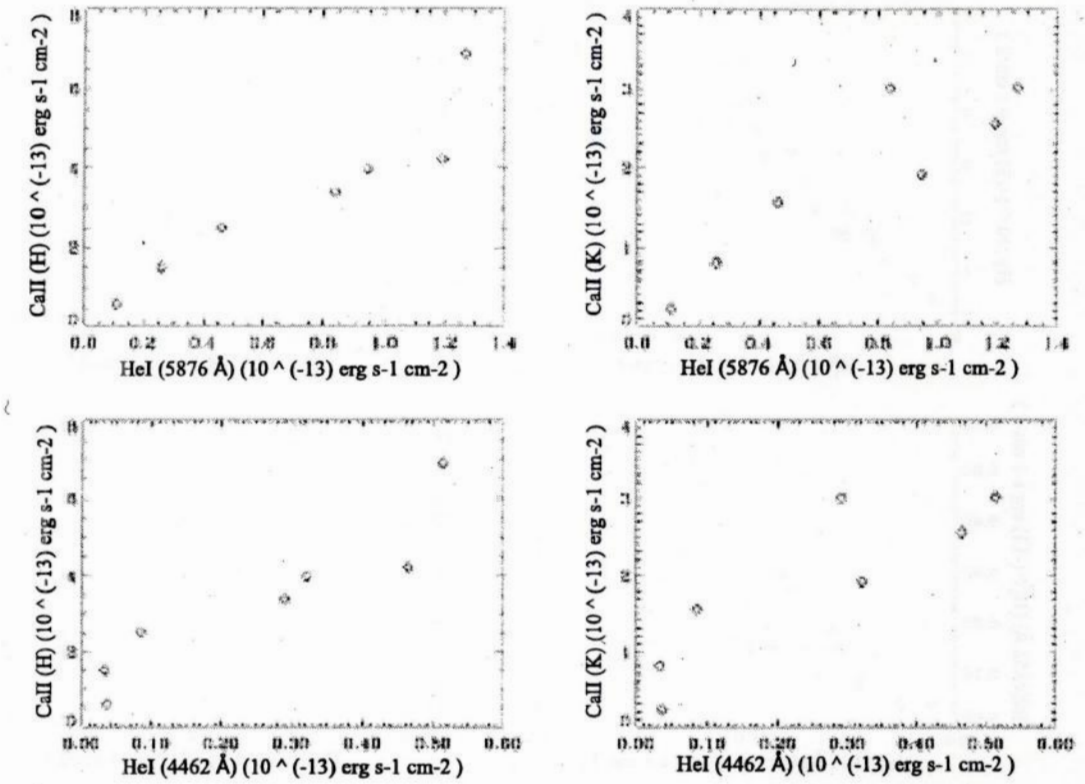

FIGURA 4.4: Correlação entre as linhas do HeI e CaII.

TABELA 4.3: Probabilidade de alarme falso entre as correlações das linhas

Linhas	Hα	HeI (5876Å)	Hβ	HeI(4462Å) (4462Å)	Hγ	Hδ	CaII (H)	CaII (K)	H8	H9	H10	H11	H12	H13
Hα	-	0.0085	0.0015	0.0272	0.0133	0.0141	0.0290	0.0061	0.0277	0.0497	0.0671	0.0914	0.0397	0.0414
HeI(5876Å)	0.0085	-	2.2×10^{-5}	6.8×10^{-6}	1.3×10^{-5}	2.9×10^{-5}	0.0020	0.0049	0.0006	0.0034	0.0050	0.0108	0.0018	0.0010
Hβ	0.0015	2.2×10^{-5}	-	0.0003	2.5×10^{-8}	0.0031	0.0130	0.0021	0.0076	0.0221	0.0427	0.0542	0.0211	0.0192
HeI(4462Å)	0.0272	6.8×10^{-6}	0.0003	-	1.3×10^{-7}	9.0×10^{-5}	0.0029	0.0112	0.0005	0.0032	0.0054	0.0104	0.0024	0.0009
Hγ	0.0133	1.3×10^{-5}	2.5×10^{-8}	1.3×10^{-7}	-	0.0004	0.0023	0.0022	0.0008	0.0043	0.0127	0.0144	0.0051	0.0042
Hδ	0.0141	2.9×10^{-5}	0.0031	9.0×10^{-5}	0.0004	-	0.0002	0.0062	1.5×10^{-5}	0.0005	0.0012	0.0027	0.0002	0.0001
CaII(H)	0.0290	0.0020	0.0130	0.0029	0.0023	0.0002	-	0.0131	1.3×10^{-5}	5.3×10^{-6}	9.3×10^{-5}	0.0001	1.2×10^{-5}	3.9×10^{-5}
CaII(K)	0.0061	0.0049	0.0021	0.0112	0.0008	0.0062	0.0131	-	0.0123	0.0286	0.0469	0.0508	0.0264	0.0202
H8	0.0277	0.0006	0.0076	0.0005	0.0008	1.5×10^{-5}	1.3×10^{-5}	0.0123	-	2.0×10^{-5}	0.0002	0.0005	2.5×10^{-5}	1.9×10^{-5}
H9	0.0497	0.0034	0.0221	0.0032	0.0043	0.0005	5.3×10^{-6}	0.0286	2.0×10^{-5}	-	1.3×10^{-5}	1.7×10^{-5}	3.9×10^{-6}	2.1×10^{-5}
H10	0.0671	0.0050	0.0427	0.0054	0.0127	0.0012	9.3×10^{-5}	0.0469	0.0002	1.3×10^{-5}	-	7.4×10^{-6}	3.9×10^{-6}	4.5×10^{-5}
H11	0.0914	0.0108	0.0542	0.0104	0.0144	0.0027	0.0001	0.0508	0.0005	1.7×10^{-5}	7.4×10^{-6}	-	5.7×10^{-5}	0.0002
H12	0.0397	0.0018	0.0211	0.0024	0.0051	0.0002	1.2×10^{-5}	0.0264	2.5×10^{-5}	3.9×10^{-6}	3.9×10^{-6}	5.7×10^{-5}	-	1.6×10^{-5}
H13	0.0414	0.0010	0.0192	0.0009	0.0042	0.0001	3.9×10^{-5}	0.0202	1.9×10^{-5}	2.1×10^{-5}	4.5×10^{-5}	0.0002	1.6×10^{-5}	-

Capítulo 5

Conclusões e Perspectivas Futuras

5.1 Análise de Periodograma

Não existe ainda um conjunto de períodos fotométricos na literatura para a estrela GQ Lupi. Covino *et al.* (1992) publicaram curvas de luz observadas durante 13 noites. Apesar de sua amostra temporal não ser adequada para uma determinação precisa do período, realizamos uma análise de periodograma nos fluxos publicados na banda V de Covino et al. (1992), utilizando o estimador de periodogramas de Scargle (1982) e atualizado por Horne & Baliunas (1986), no qual é apropriado trabalhar com dados irregularmente espaçados. A fotometria de Covino apresentou um período de 11,74 dias com PAF de 0,10.

O velamento médio de cada noite da GQ Lupi apresentou um comportamento similar ao resultado acima. Com os dados observacionais de BLB, a análise de periodograma forneceu um período de 13,093 dias com PAF de 0,001 para o velamento médio, enquanto que, em nosso trabalho a análise forneceu um período de 12,83 dias com PAF de 0,05. O grande número de observações realizadas no mês de Julho de 1998, 32 no total, é responsável pela melhor precisão na determinação do período. Na figura 5.1 observamos a variação do velamento médio ao longo das 18 noites de observação da estrela GQ Lupi.

Se consideramos que a magnetosfera estelar tem uma configuração bipolar axisimétrica onde o eixo magnético está inclinado em relação ao eixo de rotação da estrela, o gás de acresção cairá em altas latitudes. Uma vez que a estrela GQ Lupi apresenta perfis P Cygni invertido, podemos assumir que o sistema é observado com a linha de visada aproximadamente alinhada com a coluna de gás em queda livre. Assim, a variabilidade encontrada no velamento da GQ Lupi, pode estar sendo modulada pela rotação estelar fornecendo portanto um período de rotação para a estrela de aproximadamente 12 dias. Uma outra sugestão para explicar tal variabilidade é atribuída à inomogeneidades no anel

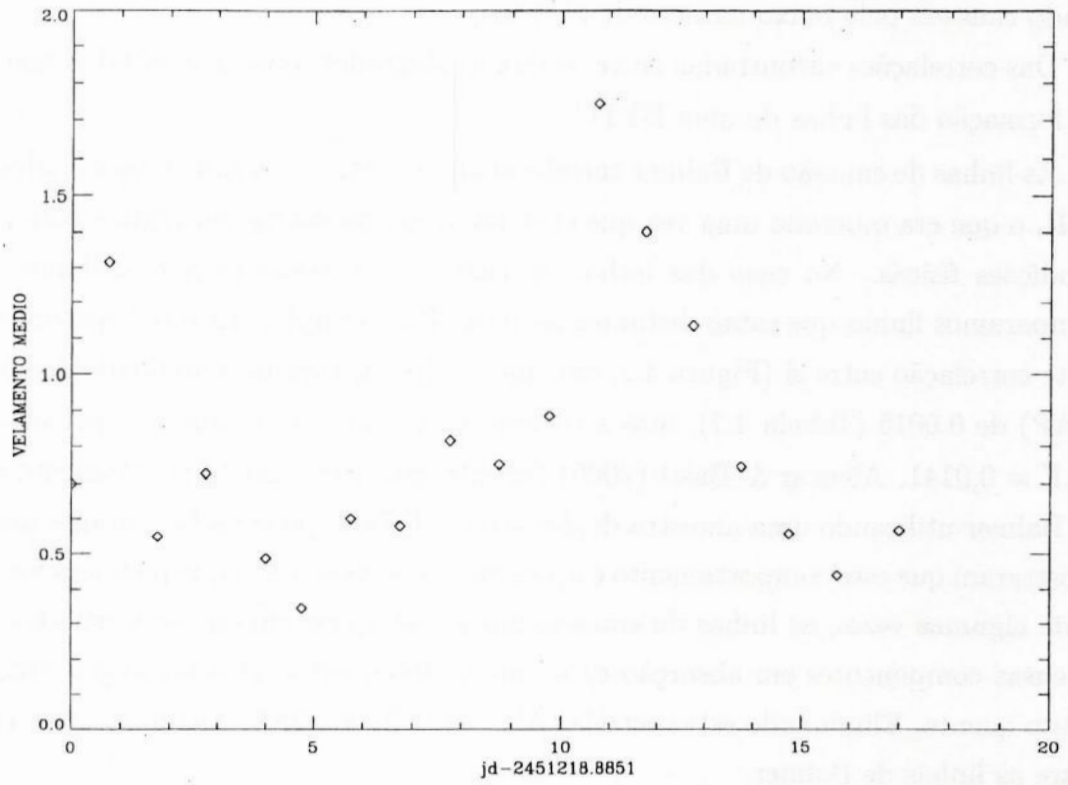

FIGURA 5.1: Variabilidade do velamento médio.

interno do disco de acresção, onde encontram-se as linhas do campo magnético estelar que irá guiar o gás do disco até a superfície da estrela. Pretendemos desenvolver modelos de região emissora para identificar quais das possibilidades governa o contínuo e as mudanças nas linhas.

As linhas de emissão não apresentaram periodicidades confiáveis. Modelos de acresção magnetosférica assumem que a estrela e a magnetosfera rotacionam juntas. As linhas de emissão surgem do funil de acresção e o velamento da região de choque próximo a superfície estelar. Esperaríamos que os fluxos das linhas apresentassem variabilidades periódicas iguais ao do velamento. Algum outro processo quase cíclico deve estar agindo na região de formação das linhas produzindo variabilidades diferentes do velamento.

5.2 Correlações

Se as linhas de emissão são realmente formadas no funil de acresção magnetosférico, esperaríamos uma correlação melhor do que foi encontrado entre os fluxos integrados das linhas e o velamento. Apenas Hβ, Hγ e HeI (4462 Å) apresentaram boas correlações com o velamento. A princípio, a aparente falta de correlação com as demais linhas pode estar

sendo causada pelo baixo número de observações.

Das correlações encontradas entre os fluxos integrados, podemos inferir vários aspectos da formação das linhas de uma ETTC.

As linhas de emissão de Balmer correlacionam-se entre si, assim como as linhas do HeI e CaII, o que era esperado uma vez que elas devem ser formadas em regiões com as mesmas condições físicas. No caso das linhas de Balmer, a correlação parece diminuir quando comparamos linhas que estão distantes na série. Por exemplo, Hα e Hβ apresentaram uma forte correlação entre si (Figura 4.2, em cima à direita) com probabilidade de alarme falso (FAP) de 0,0015 (Tabela 4.2), mas a correlação de Hα e Hδ diminuiu, apresentando uma PAF = 0,0141. Alencar & Basri (2000) encontraram o mesmo comportamento das linhas de Balmer utilizando uma amostra de 30 estrelas T Tauri observadas durante uma década. Mostraram que esse comportamento é apresentado pelas estrelas que possuem fortes ventos, onde algumas vezes, as linhas de emissão quase não aparecem em seus espectros devido a intensas componentes em absorção e/ou um contínuo sendo produzido por uma fotosfera muito quente. Eliminando estas estrelas Alencar & Basri (2000) melhoraram as correlações entre as linhas de Balmer.

As linhas de HeI se correlacionam bem entre si (Figura 4.2, em baixo à esquerda, PAF = 6,762 x 10^{-6}). Elas também apresentaram boas corelações com a série de Balmer. No entanto, foram com as linhas Hβ, Hγ e Hδ que as do HeI obtiveram as melhores correlações (Figura 4.3, em cima). A menor correlação com as demais linhas parece ser devido a um número pequeno de observações, apesar de Hδ estar incluída nesse grupo. Acredita-se que as linhas do HeI são formadas em regiões de altas temperaturas (20000 a 50000K) e junto com o tamanho de sua componente larga sugerem que essas linhas são formadas no funil de acresção magnetosférico próximo a região de choque.

Acredita-se que as linhas H & K do CaII também são formadas no funil de acresção. Essas linhas apresentaram boas correlações com as linhas de Balmer e do HeI. As correlações entre os fluxos integrados das linhas de emissão, favorecem os modelos de acresção magnetosférica como sendo o principal mecanismo responsável pelas variabilidades encontradas na estrela GQ Lupi.

5.3 Perspectivas Futuras

Daremos continuidade ao projeto de variabilidade de estrelas T Tauri clássicas que resultará numa tese de mestrado. O projeto terá os seguintes passos:

a) comparar os perfis de Balmer de 1998 (BLB) com aqueles de 1999 e

b) procurar explicar a melhor configuração de gás responsável pelas características

espectrais observadas nestes perfis. Para isso, utilizaremos modelos de perfis recentemente publicados por Muzzerole e Calvet (2000).

Bibliografia

[1] Alencar, S.H.P., & Basri, G. 2000, A.J., 119,1881

[2] Alencar, S.H.P., Johns-Krull, C.M., & Basri, G. 2001, A.J., 122, 3335

[3] Basri, G., & Batalha, C. 1990, Ap.J., 363, 654

[4] Batalha, C., Lopes, D.F., & Batalha, N.M. 2001, Ap.J., 548, 377 (BLB)

[5] Bertout, C. 1989, Ann. Rev. Astr. ap., 27, 351

[6] Bevington, P.R. 1969, Data Reduction and Error Analysis for the Physical Sciences (New York: McGraw-Hill)

[7] Calvet, N., & Hartmann, L. 1992, Ap.J., 386, 239

[8] Camenzind, M. 1990, Reviews in Modern Astronomy (Springer-Verlag: Berlin), 3, p. 234

[9] Covino, E., Terranegra, L., Franchini,M., Chavarria, K., & Stalio, R. 1992, A&AS, 94, 273

[10] Edwards, S., Hartigan, P., Ghandour, L., & Andrulis, C. 1994, A.J., 108, 1056

[11] Filippenko, A.V. 1982, PASP, 94, 715

[12] Hartmann, L., Hewett, R., Stahler, S., & Mathieu, R.D. 1986, Ap.J., 309, 275

[13] Hartmann, L., Hewett, R., & Calvet, N. 1994a, Ap.J., 426, 669

[14] Herbig, G.H. 1960, Ap.JSupp., 4, 337

[15] Herbig, G.H., & Bell, K.R. 1988, Third Catalog of Emission-Line Stars of the Orion Population, Lick Observatory Bulletin No. 1111 (HBC) Hillenbrand, L.A., Strom, S.E., Vrba, F.J., & Keene, J. 1992, Ap.J., 397, 613

[16] Horne, J.H., & Baliunas, S., L. 1986, Ap.J., 302,757

[17] Johns-Krull, C.M., & Basri, G. 1997, Ap.J., 474, 433

[18] Joy, A.H. 1945, Ap.J., 102, 168

[19] Kenyon, S.J., & Hartmann, L. 1995, Ap.JSupp., 101, 117

[20] Konigl, A. 1991, Ap.J. Lett., 370, L39

[21] Lada, E.A., Evans, N.J. II, Depoy, D.L., Gatley, I. 1991, Ap.J., 371, 171

[22] Lynden-Bell, D., & Pringle, J.E. 1974, M.N.R.A.S., 168, 603

[23] Moore, C.E., Minnaert, M.G.J., & Houtgast, J. 1966, The Solar Spectrum 2935Å to 8770Å (NBS Monograph 61)(Washington: NBS).

[24] Valenti, J.A. 1994, Ph.D. thesis, Univ. of California, Berkeley

Apêndice A

Artigo - Variability of Southern T Tauri Stars (VAST) III: The Continnum Flux Changes of The TW Hya Bright Spot)

Variability of Southern T Tauri Stars (VASTT) III: The Continuum Flux Changes of the TW Hya Bright Spot [1]

Batalha, C.[1], Batalha, N.M.[2], Alencar, S.H.P.[3], Lopes, D. F.[1] & Duarte, E.S.[1]

ABSTRACT

We have collected low resolution spectrophotometric data of the classical T Tauri star TW Hya in an effort to detect and to follow the excess continuum emission (veiling) and the line changes at $\lambda < 5100$ Å. The de-veiled and calibrated flux distribution resembles that of a 30 Myr K7-M1 star, of radius $R/R_{\odot} = 0.8$, mass $M/M_{\odot} = 0.7$ and $\log g = 4.5$. The anticorrelation between the veiling (in the B-band) and the observed Balmer jump, found by previous authors based on large samples of classical T Tauri stars, is confirmed in TW Hya. The line emission luminosities of the H, CaII and HeI lines correlate with one another throughout the series, supporting the claims that the bulk of the line emission is formed in a single region or their growth is controlled by a common mechanism. Surprisingly, the line emission fluxes do not correlate with the veiling at 4250 Å (B-band). The line luminosities are in general less than 1% of the continuum luminosities.

The veiling time series presents a cyclic behavior at 4.4 ± 0.4 days. We collect all of the archival photometric data and analyze the B-band observations using different algorithms. We found solutions at either the 4.4-day timescale or one half of this value. The data sets presenting the 2.2-day periodicity yield double-peaked light curves when folded at the 4.4-day timescale. We interpret the 4.4 days solution as the rotation period of the star.

---

[1]Observatório Nacional/CNPq, Rua General José Cristino, 77, Rio de Janeiro, RJ 20920-400, Brazil,

celso@on.br

esduarte@on.br

dalton@on.br

[2]NASA Ames Research Center, Planetary Systems Branch, Moffett Field, CA 94035-1000, USA,

natalie@pollack.arc.nasa.gov

[3]Universidade de São Paulo, IAG, Departamento de Astronomia, Rua do Matão, 1226, São Paulo, 05508-900, Brazil,

alencar@astro.iag.usp.br

The veiling and the line emission measurements yield accretion luminosities for the series. We model the impacted area in the photosphere by an isothermal gas of a given density, temperature and size (δ) whose parameters change as the star rotates. Estimations of the total spot area (δ), as a percentage of the stellar projected area, lie within the range $2.5 < \delta < 6.0$. The accretion luminosity of the impacted region does not remain constant throughout the series. The mass accretion rate ($\dot{M}_{acc}$) that governs the luminosity, varies within 1.0×10^{-9} $M_{\odot}yr^{-1} < \dot{M}_{acc} < 4.8 \times 10^{-8}$ $M_{\odot}yr^{-1}$. The spot luminosity and the associated $\dot{M}_{acc}$ are tightly correlated to the projected spot area, δ, and change their absolute value as the star spins. If most of the accretion is channeled to a single spot, its colatitude will be larger than 70°, indicating that the magnetic dipole is largely inclined.

Subject headings: Accretion, accretion disks – stars: T Tauri, pre Main Seqüence – stars: YY Ori, individual (TW Hya)

1. Introduction

TW Hya has been extensively studied during the past few years, following the gradual disclosure of its observational and intrinsic characteristics. It is one of the closest ($\sim$ 56 pc; Whichmann et al. 1998) and one of the oldest ($\sim$ 10M yr; Webb et al. 1999) classical T Tauri stars (CTTS), showing one of the strongest hydrogen emission measures ($EW_{H\alpha} \sim 200$ Å, Herbig & Bell 1988). It is one magnitude brighter than most of the well–studied CTTS ($V < 11.5$), which explains its presence in many related observing programs. Originally, TW Hya was considered a fine example of an isolated, active pre–main sequence star separated from any known site of star formation (Rucinski & Krautter 1983). The identification and classification of optical counterparts to IRAS sources (de la Reza et al. 1989; Gregorio-Hetem et al. 1992), together with proper motion studies of nearby optical sources (Webb et al. 1999), revealed, on the contrary, the presence of several young objects in the vicinity of TW Hya, which is now recognized as the brightest optical member of an association. Currently, the TW Hya association is comprised of 21 stars, six of which are resolved binary systems, including one brown dwarf and two CTTS (Webb et al. 1999; Zuckerman et al. 2001; Sterzik et al. 1999).

The proximity of TW Hya motivated several attempts at direct disk imaging. The typically narrow molecular emission lines (< 1 km s^{-1}) and the apparent lack of circumstellar gas led Kastner et al. (1997) to suggest that a nearly face-on dusty molecular disk surrounds TW Hya. Wilner et al. (2000) imaged the circumstellar structure of TW Hya with the millimetric interferometry

---

[1]Based on observations taken at the European Southern Observatory, La Silla, Chile, under the bilateral ESO - Observatório Nacional agreement

technique available at the Very Large Array. Their resulting 7 mm image was also consistent with a face-on disk. Hubble Telescope R and I images provided further evidence for a face-on disk (Krist et al. 2000). More recently, Potter (private communication) observed a symmetric structure around TW Hya with H-band dual imaging polarimetry and estimated a disk inclination between 5° and 15°.

The disk accretion of CTTS starts decaying at about 5 million years in Chamaeleon and Taurus Aurigae (Brandner et al. 2000; Strom et al. 1993) two of the closest and well studied star formation complexes (d $\sim$ 150 pc). Few CTTS are then left to reveal the advanced stages of disk evolution where planet formation becomes operational. As one of the closest, brightest, and oldest CTTS with significant Balmer emission, TW Hya is a convenient laboratory to constrain models of disk evolution and to probe an important phase of planet building.

Disk accretion properties can be inferred from the Balmer line strength (Hartmann et al. 1994) which is conspicuously strong in TW Hya, and by modeling the optical energy distribution (Muzerolle et al. 2000) which is easily accessible for a star of V = 11.5 mag. The current models state that a CTTS consists of a low mass star surrounded by a strong bipolar magnetosphere that truncates the accreting disk at few stellar radii near the corotational radius. Disk material is lifted off the disk plane and is guided towards high latitude regions of the central star (Königl 1991). The falling gas crashes against the stellar surface, releasing the kinetic energy in X-rays and UV radiation, which is further reprocessed as the so called optical veiling in the underlying photosphere (Calvet & Gullbring 1998). A natural consequence of this paradigm is the development of hot rings or spots sitting near the rotational poles. If the magnetosphere is tilted with respect to the rotational axis or if the accretion is not axisymmetric, the photometric light curve will modulate as the star rotates (Mahdavi & Kenyon 1998).

The first detailed photometric monitoring of TW Hya indicated color gradients consistent with rotational modulation of hot spots (Rucinski & Krautter 1983). In addition, short term variability with time scales of 0.2 days were seen superimposed on the light curve, leading Herbst & Koret (1988) to suggest that a hot spot was controlling the TW Hya light curve. They submitted their photometry to a periodogram analysis, and obtained two solutions at 1.28 and 4.5 days. They favored the former as being more consistent with the detected robust short term variability and interpreted the 4.5 day solution as the beat period to the 1.28 day solution. Their spot models yielded fractional areas of 1% with typical temperatures of 8800 K. Herbst & Koret (1988) also submitted Rucinski & Krautter (1983) photometry to a periodogram analysis and detected two peaks in the power spectra at 1.8 and 2.25 days. Again, they suggested that the second solution is the beat period of the short period and real solution (1/1.8 + 1./2.25 $\sim$ 1/1). A more recent photometric time series (Mekkaden 1998) confirmed the presence of a hot spot with temperature of 8450 K and covering 0.1% of the stellar disk. Mekkaden analysis suggested a periodic light curve of 2.196 days. The apparent discrepancies among the published rotational periods leaded Kastner et al. (1999) to examine the archival photometry of Hipparcos. They concluded that none of the previously suggested periods could be verified with the Hipparcos data. They argued that

the published short period solutions were not compatible with the face-on disk orientation of TW Hya (Kastner et al. 1997; Krist et al. 2000; Wilner et al. 2000), unless abnormally large equatorial velocities were envisioned for this star, which has vsini $\sim$ 5 km s^{-1} (see Alencar & Batalha 2002 - VASTT2 henceforth). In conclusion, the available photometry provides strong support for hot spots controlling the short and long term variabilities. Nevertheless, the lack of a unique period solution (1.28 days, 1.8 days and 2.196 days) has been a hindrance for vindicating rotational modulation of the light curve as the dominant mechanism governing the proposed cyclic behavior.

The accretion signature cannot be modeled in detail by blackbodies (Calvet & Gullbring 1998; Valenti et al. 1993) – the standard approach to interpret color gradients established photometrically – and an improved model of the spectral energy distribution is needed. Costa et al. (2000) analyzed the UV spectra of a weak-lined, a moderate and a CTTS (TW Hya), and showed that their respective ultraviolet continuum distribution is fitted by a hydrogen free-free plus free-bound gas emission of 1 to 5 $\times$ 10^4 K, which had to be added to the cool underlying photosphere. Of the three stars, TW Hya required an additional 7900 K blackbody emission covering 5 % of the stellar surface. This blackbody radiation is added to the photospheric flux distribution, diminishing the depth of absorption lines. The weakening of the absorption lines is technically called optical veiling, which is here defined as the ratio between the blackbody flux excess and the continuum photospheric flux. The model parameters suggested by Costa et al. (2000) yielded a spectral veiling of 1.0 at Hα, which is comparable to the largest high resolution veiling measured for TW Hya (Alencar & Batalha 2002). The accretion shock model of Calvet & Gullbring (1998, CG98 henceforth) applied to this 10 Myr CTTS (Muzerolle et al. 2000) predicted a filling factor one magnitude smaller (0.3%) than the Costa et al. (2000) results. The model of Muzerolle et al. (2000) predicted the UV/optical continuum and the veiling at 7000 Å (r_λ = 0.27) consistent with the observations. In spite of predicting the observable veilings, the UV model of Costa et al. (2000) and the shock model of Muzerolle et al. (2000) suggest total spot areas differing by a factor of 10.

It is conceivable that the star/disk system experiences dramatic changes from time to time, and the extreme values of the spot parameters predicted by different models reflect real and extreme differences of the star/disk environment. On the other hand, it is possible that different models when applied to the same set of data predict incompatible values, revealing a structural problem with one of the models. In this regard, the robustness of a given model can be better tested if it predicts the behavior at different phases of a given object, assuming variability is primarily rotationally induced. If the star/disk system goes through extreme changes one will be able to trace the past history leading to the abrupt change. A good scenario that explains one particular observing phase should be able to explain all the other ones. This discussion reinforces the importance of continued monitoring of individual CTTS, specially when absolute flux calibration is achieved. We present low resolution time series of TW Hya in an effort to add further constraints to TTS models in general, specially for stars such as TW Hya that are in the final phases of disk accretion.

2. Observations

The observations were done with the ESO 1.52 m telescope at La Silla with the Boller & Chivens spectrograph. The spectral format was chosen to include important variable lines, such as the high Balmer and the CaII H & K lines, as well as the continuum regions most sensitive to changes of hot spots. The chosen region includes the U and B broad bands and covers the spectral range of 3100 Å $< \lambda <$ 5100 Å. The spectrograph feeds a Loral Lesser CCD instrument (2048 x 2048) and provides an effective resolution of 2 Å. A total of 19 spectra were obtained during 6 nights in May and 8 nights in July 1998. Data reduction and spectrophotometric calibrations are performed in a standard way, following the steps explained in Batalha et al. (2001, VASTT1 henceforth). As commented in VASTT1, the nights were not always photometric, and this prevented us from making a self–consistent determination of the stellar radius and the circumstellar extinction for some program stars. In spite of the variable atmospheric transparency in some of the TW Hya exposures, we flux calibrated all the exposures to recover the shape of the systemic spectral energy distribution (star + disk accretion = SED). By assuming that high clouds would gray shift the systemic SED but preserve its shape, the actual observed and gray shifted SED can be used to constrain models of the continuum emitting regions, such as those developed in Section 4.1. We present, in Table 1, the observation journal along with line emission measurements described in Section 3.2.3.

Some of the exposures were taken on nights with optimal sky conditions, allowing us to access the TW Hya reddened photosphere after performing the veiling subtractions (see Section 3.1 for details). We compare this particular sample of spectrophotometric data with the previously published photometry of TW Hya, after convolving the spectrophotometry with the broad-band filter response curves (Budding 1993). The computed U and B-band magnitudes are displayed in Figure 1 **a** and **b**, respectively. The average magnitude levels are comparable to those of previous photometry, indicating similar degrees of activity at these epochs. The Balmer continuum fluxes reveal variances that are larger than those of the Paschen continuum adjacent to the jump.

The choice of a proper template is relevant for veiling determination and for providing a reliable set of gas parameters representative of the reprocessed gas atmosphere. We compare the ratios of several blended absorption lines in the TW Hya spectra with those measured in several main sequence stars, including cool members of the Jacoby et al. (1984, JHC84) library. We find that the star BD+63^o 0137, listed as dM1 in the JHC84 library, is the ideal match to TW Hya (classified as a K7 V in the Herbig & Bell (1988) catalog). The match is even better than that obtained with a K7 V Gliese star (GL 825) observed with the same settings. We further investigate the spectral classification of TW Hya using some of the high resolution (FEROS) data described in Alencar & Batalha (2002). We compute the quadratic differences between samples of normalized TW Hya FEROS spectra with those of several artificially veiled Gliese stars. The chosen (veiled) template is the one showing the smallest residuals. We conclude that GJ 1172, a K7 V star, is the best match to TW Hya, supporting the earlier Herbig & Bell (1988) spectral classification. It is possible then, that BD+63^{o}013 is mis-classified in the JHC84 library. In fact, Montes & Martin

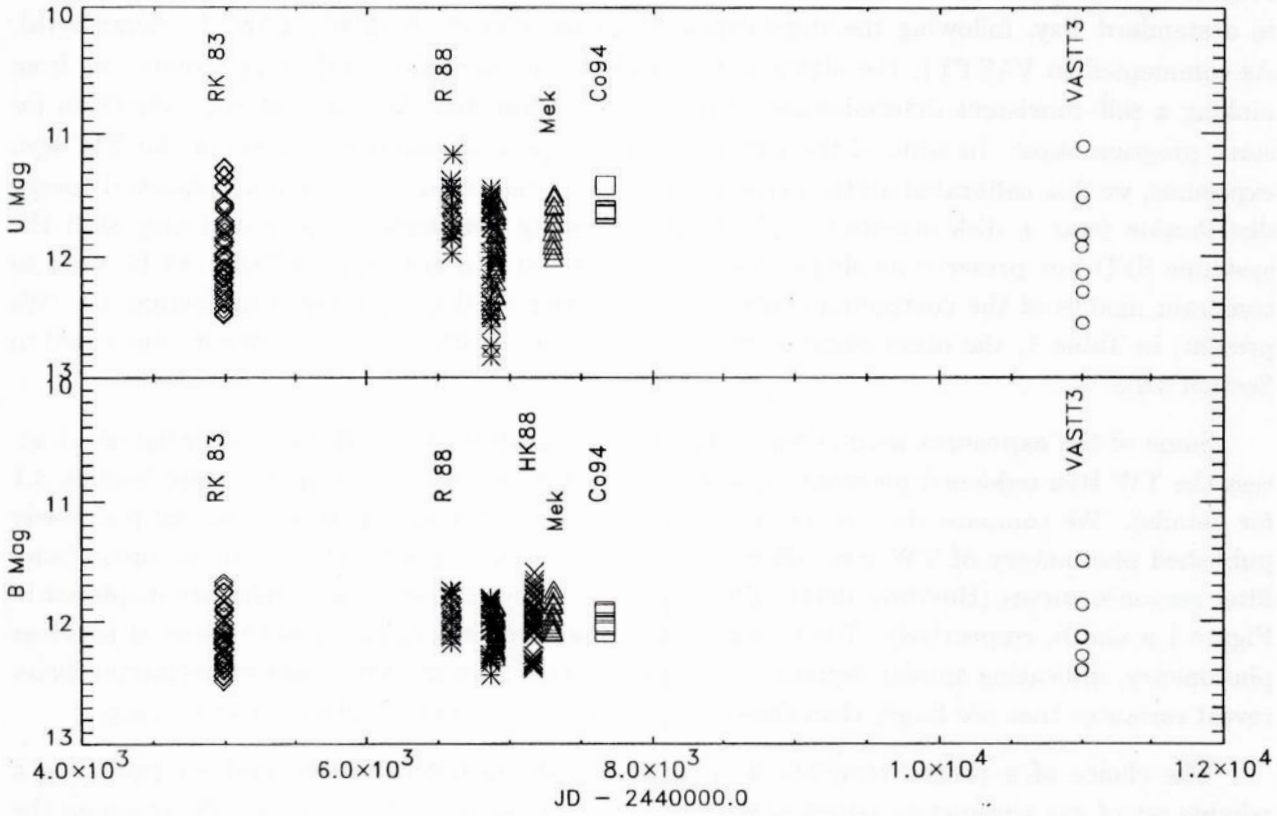

Fig. 1.— Photometric data of Rucinski & Krautter (1983, RK83), Rucinsky (1988, R88), Mekkaden (1998, M98), Herbst & Koret (1988, HK88) and Covino et al. (1994, Co94) in the U (**a**) and B broad-bands (**b**) are compared with our synthesized photometry (VASTT3).

Table 1. Line Fluxes, Equivalent Widths and Continuum Emission of TW Hya. The fluxes are in units of 1.0×10^{-12} erg cm^{-2} s^{-1} and the HeI line is at 4471 Å

JD -2450000	F Hβ	W Hβ	F HeI	W HeI	F Hγ	W Hγ	F Hδ	W Hδ	F +Hε	W +Hε	F K	W K	F H6	W H6	F H7	W H7	F H8	W H8	F H9	W H9	F H10	W H10	F H11	W H1 1	F H12	W H12	F H13	W H13	F H14	W H1 4	r_{3550}	r_{4250}	r_{4800}
941.479	3.5	23.7	1.29	0.93	1.9	16.7	1.3	12.8	1.3	13.9	0.4	4.7	0.8	9.0	0.6	6.9	0.5	5.2	0.3	3.7	0.3	2.7	0.2	2.1	0.1	1.2	0.1	0.9	0.1	0.6	8.5	2.4	0.8
941.575	4.0	31.1	0.99	0.80	1.7	16.0	1.1	11.1	1.0	11.9	0.4	4.5	0.7	7.8	0.5	5.5	0.4	4.3	0.3	3.2	0.2	2.5	0.2	2.2	0.1	1.3	0.1	1.0	0.1	0.6	8.0	2.3	0.8
941.679	5.0	36.6	1.23	0.93	2.0	17.2	1.3	12.1	1.2	11.6	0.5	5.0	0.8	7.7	0.6	6.5	0.5	4.6	0.4	3.5	0.3	2.9	0.2	2.5	0.2	1.7	0.1	1.1	0.1	0.7	7.5	2.4	0.8
942.492	5.2	55.8	1.2	1.39	2.3	33.5	1.6	26.4	1.6	32.9	0.5	12.5	1.0	21.9	0.8	16.9	0.7	13.8	0.5	10.6	0.4	8.5	0.4	7.1	0.3	4.5	0.2	3.0	0.1	1.9	6.5	1.1	0.4
942.546	5.9	54.9	1.14	1.16	2.5	32.3	1.5	22.5	1.5	27.1	0.5	9.7	0.9	17.0	0.8	13.7	0.6	10.8	0.5	8.4	0.4	7.8	0.3	5.6	0.2	3.5	0.2	2.8	0.1	1.7	6.0	1.3	0.5
942.670	6.4	68.5	1.39	1.76	2.5	43.0	1.5	28.5	1.6	39.3	0.6	14.7	1.0	24.1	0.9	24.0	0.7	19.3	0.6	15.0	0.5	13.5	0.5	13.1	0.3	6.9	0.2	4.8	0.2	2.8	6.5	1.0	0.1
943.486	10.4	83.1	2.48	2.38	4.3	52.9	2.9	43.8	2.9	56.9	0.9	18.1	1.9	38.1	1.6	31.1	1.3	27.0	1.0	18.6	0.9	15.7	0.7	11.4	0.5	7.2	0.3	4.0	0.2	2.3	9.0	1.2	0.8
944.669	5.0	34.0	1.45	1.04	2.2	1.04	1.6	14.6	1.6	16.5	0.5	5.1	1.0	10.3	0.8	8.2	0.6	6.3	0.5	5.3	0.4	4.0	0.3	2.9	0.2	1.8	0.1	1.0	0.1	0.5	8.5	2.5	0.6
945.555	3.4	27.9	1.09	0.95	1.6	16.2	1.1	12.6	1.1	14.5	0.3	4.9	0.7	9.1	0.5	7.2	0.4	5.6	0.3	4.1	0.2	3.0	0.2	2.5	0.1	1.4	0.1	1.0	0.1	0.6	7.0	2.1	0.4
947.529	6.2	58.4	1.52	1.59	2.5	30.8	1.6	22.1	1.7	25.6	0.5	8.5	1.1	16.5	0.9	13.6	0.7	10.5	0.6	8.9	0.5	7.5	0.4	5.3	0.3	3.8	0.2	2.4	0.1	1.5	8.5	1.6	0.8
997.487	5.4	67.3	1.96	2.55	2.6	46.6	1.8	41.5	1.7	53.0	0.6	23.9	1.1	42.4	0.9	33.8	0.8	30.1	0.7	25.4	0.6	22.0	0.5	15.9	0.4	10.3	0.3	6.0	0.2	3.4	7.0	0.6	0.3
998.487	5.5	57.8	1.37	1.54	2.6	36.0	1.7	28.3	1.6	35.6	0.6	13.5	1.0	23.7	0.8	19.6	0.6	15.3	0.5	12.0	0.4	9.5	0.3	7.1	0.2	4.7	0.2	3.1	0.1	1.9	6.0	1.1	0.4
999.527	4.0	27.5	1.13	0.77	1.7	13.5	1.1	9.4	1.1	10.4	0.4	3.8	0.6	6.4	0.5	5.3	0.4	3.7	0.3	3.0	0.3	3.0	0.2	2.2	0.1	1.2	0.1	0.9	0.0	0.5	9.0	2.9	0.9
1000.477	2.8	23.4	1.09	1.00	1.6	17.5	1.2	14.7	1.2	17.8	0.3	5.5	0.7	11.7	0.6	10.4	0.5	7.2	0.3	5.1	0.2	3.9	0.2	2.9	0.1	1.5	0.1	1.1	0.0	0.5	5.5	1.7	0.6
1001.466	2.3	22.4	0.76	0.846	1.4	21.0	1.1	20.2	1.1	28.2	0.3	10.6	0.7	19.9	0.6	17.9	0.5	12.7	0.4	9.6	0.2	6.8	0.2	4.4	0.1	2.3	0.1	1.7	0.0	0.9	3.7	0.9	0.2
1002.471	4.4	49.8	0.84	1.03	1.9	31.0	1.2	26.1	1.2	35.1	0.4	13.9	0.8	24.8	0.6	20.3	0.5	15.1	0.4	11.8	0.3	8.5	0.2	6.0	0.1	3.6	0.1	2.4	0.0	1.1	4.0	0.6	0.3
1002.576	5.6	55.4	0.66	0.703	2.1	30.1	1.3	23.6	1.2	31.4	0.4	11.8	0.8	21.9	0.6	17.9	0.4	13.1	0.3	10.1	0.3	8.2	0.2	6.6	0.1	3.9	0.1	2.7	0.1	1.4	3.1	0.8	0.3
1003.465	7.9	67.9	1.39	1.247	3.0	32.3	1.8	22.7	1.8	27.6	0.6	9.6	1.1	17.5	0.8	13.4	0.7	10.7	0.5	8.2	0.4	7.0	0.4	5.5	0.2	3.6	0.2	2.6	0.1	1.6	8.0	1.7	0.6
1004.453	7.5	55.1	2.21	1.66	3.4	28.5	2.2	20.9	2.1	21.9	0.7	7.6	1.4	15.2	1.1	12.7	0.9	9.8	0.7	7.8	0.6	6.2	0.4	4.6	0.3	3.1	0.2	2.0	0.2	1.4	9.5	2.4	0.8

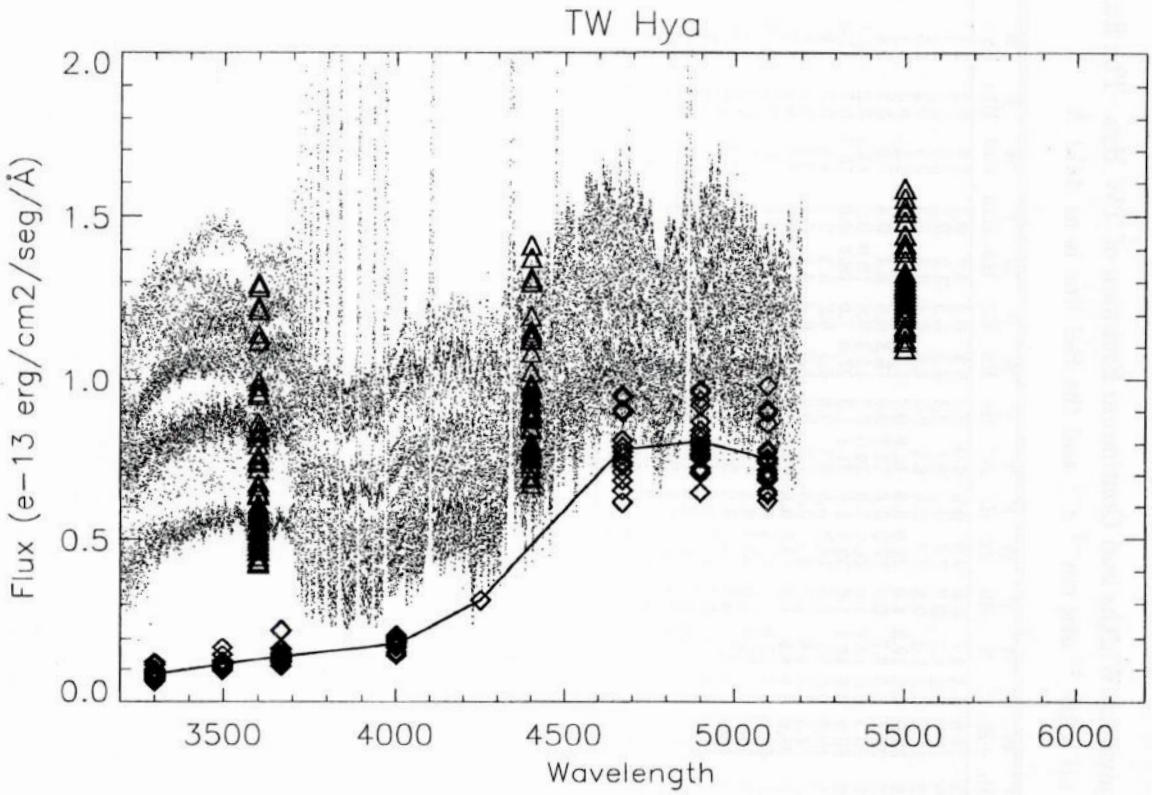

Fig. 2.— The observations obtained through clear sky are used to compute the fiducial TW Hya photospheric distribution (described in Section 3.2). All the other *photospheres* (diamonds) are normalized to the resulting fiducial TW Hya photosphere at 4250 Å (thick line), and their flux calibrated distributions (dots) are displayed along with Rucinski & Krautter (1983) photometry (triangles).

(1998) classify BD+63^{o}013 as a K7 star, using a high resolution library of echelle spectra, which further motivates us to adopt this star as a template of the TW Hya photosphere. We degrade our data to the nominal resolution of 4 Å (see JHC84) and compute the veiling time series as described in Section 3.2.1.

3. Results

3.1. The Flux Calibration

Some of our data are not of photometric quality preventing a direct determination of the stellar parameters. However, subtracting the veiling distribution from the observed SED yields the (reddened) photospheric SED, depleted by a weather–dependent factor. A first attempt to convert our data into absolute flux units is presented in Batalha & Batalha (2001). The 19 exposures are de-veiled, normalized to the brightest and the resulting mean curve adopted as the TW Hya photospheric flux distribution. This method implicitly assumes that the nightly sensitivity functions are well determined in all observing nights. Here we adopt a more conservative approach selecting only data from the best nights. Thus, we subtract the spectral veiling distribution (see Section 3.2.1) from the 7 observations acquired under ideal sky conditions throughout the night (see Figure 2) and determine the photospheric flux level after averaging. Our dominant source of error is the veiling (r_λ) itself, to which we assign an uncertainty of $\pm$ 0.5 for $\lambda > 4000$ Å (see VASTT1). This yields $\sigma/F_{cont} \sim 0.5/(1. + r_\lambda)$, which is less than 0.5 throughout the spectrum. In fact, all the resulting 7 *photospheres* deviate less than 30% from their average. By establishing where the TW Hya photosphere is, all the other spectra taken under unfavorable sky conditions can be properly corrected by repeating the steps outlined above. The gray shifting factors are those that bring the individual and gray shifted photospheric flux distribution to the fiducial photosphere at 4250 Å. The latter can be easily accessed by reading the star BD+63^o 013 from the JCH84 library and applying the factor 0.095 on the distribution.

Naked T Tauri stars (NTTS) are low mass pre-main sequence stars that show no indication of disk accretion. Therefore, the atmosphere of a NTTS is the ideal candidate to mimic the atmosphere of a CTTS, specially if target and template are located in the same star formation complex. However, stellar activity declines with age, and magnetic active regions are expected to populate the surface of a late type pre-main sequence star. In fact, the Herbst et al. (1994)'s photometric catalog indicates that cool spots, in general, modulate the light curves of a NTTS to a few tenths of a magnitude with an upper limit of 0.8 mag. Then, it is possible that flux gradients governed by cool spots drive the observed TW Hya colors, and compete with the accretion signature in controlling the observed light curve. Thus, it should be kept in mind that our procedure of normalizing each individual reddened photosphere to the brightest is subjected to an uncertainty we are unable to quantify. Implicitly, we assume that the photosphere is free from spots cooler than the photosphere and the impacted hot region is alone providing modulations in the light curve.

Figure 2 shows the shifted (diamonds) and the fiducial TW Hya (solid lined) photospheres. The systemic distributions (photosphere + optical excess emission) are displayed for reference (dotted lines). The photometric broad band fluxes of Rucinski & Krautter (1983) are presented for comparison (triangles). Our weather corrected and flux-calibrated data is compatible with those obtained in previous photometric campaigns, providing strong support to the photospheric distribution we claim.

The TW Hya spectral energy distribution is expected to suffer negligible extinction because the star is sufficiently close (d $\sim$ 56 pc - Wichmann et al. 1998) and is not immersed in any molecular cloud. In fact, previous determinations of the circumstellar extinction confirms this hypothesis ($A_V < 0.25$, Costa et al. 2000; $A_V = 0.0$, Blondel et al. 1993; Muzerolle et al. 2000). The ISM extinction coefficients of Cardelli et al. (1989) are used to de-redden the observed photospheric flux until the resulting distribution matches that of the adopted template. We estimate a circumstellar extinction of $A_V = 0.1 \pm 0.1$ mag, in accordance with previous determinations. The de-reddened photospheric flux distribution is extrapolated towards the infrared, guided by the spectral distribution of a K7 dwarf (Johnson 1966), to compute the bolometric flux. The derived stellar luminosity is used to estimate the stellar parameters (Table 2) after positioning the star in the theoretical H-R diagram of Baraffe et al. (1998). As can be seen in Table 2, TW Hya seems to be slightly more evolved than previously thought and has an estimated radius of R = 0.8 $R_\odot$.

We emphasize the importance of the veiling subtraction along with extinction corrections to properly place a CTTS in the HR diagram. Our procedure incorporates a thorough veiling correction, which decreases the intrinsic stellar luminosity and increases its age to 30M years. An upper limit to the total photospheric flux can be obtained by integrating the available UBVRIJHKL fluxes. Here, veiling is implicitly incorporated into the energy budget as well as the disk reprocessed stellar light and the gas viscous dissipation in the disk. Rucinski & Krautter (1983) photometric data is integrated, and a total *photospheric* flux of 2.3×10^{-9} erg cm^{-2} s^{-1} is found, which is 0.2 dex larger than the value reported in Table 2 that includes veiling corrections. The corresponding stellar radius and age are consistent with those reported previously by Webb et al. (1999) and confirmed by Weintraub et al. (2000), e.g. $\sim$ 1.0 $R_\odot$ and 10 Myr. This exercise indicates that the continuum excess emission should be taken into consideration prior to positioning a classical TTS such as TW Hya in the HR diagram.

Table 2. Stellar Parameters of TW Hya

SpT	A_V	$R/R_\odot$	$M/M_\odot$	$\log g$	$\log L/L_\odot$	Age (Myr)
K7-M1 V	0.1±0.1	0.8	0.7	4.5	-0.8	30

3.2. The Night-to-Night Variability

3.2.1. The Veiling

The excess continuum emission from independent line blends (at low resolution) is readily retrieved by artificially veiling the template BD+63°013 until a match between the veiled template and the CTTS is obtained. The list of photospheric absorption features used includes a) a strong blend of low excitation iron lines at 3550 Å, which yields a single but firm constraint to the Balmer continuum emission models discussed in Section 3.4, b) the TiO molecular band at 4750 Å, which supports a later spectral – type classification, and c) several other minor absorption lines. We refer to VASTT1 for further details on the veiling determination procedure. Veiling measurements of four exposures that show extreme (low and high) Balmer jump sizes (see section 3.2.2) are displayed as asterisks in the right panels of Figure 3.

The night-to-night changes of the 4000 Å veiling for the May and July runs are presented as filled circles in Figure 4. The veiling amplitudes in both months are comparable and show a quasi sinusoidal behavior. The veiling changes from about 1.5 to 4.5 and never completely fades, indicating that at least some part of the impacted region is always in view as the star rotates. The current paradigm for magnetically controlled disk accretion assumes an axisymmetric configuration for the magnetosphere. Thus, if the light curve changes are being governed by accreting hot ring/spots, the magnetic axis must be tilted with respect to the stellar axis of rotation. Given the fact that the star-disk system is nearly pole-on (Krist et al. 2000; Wilner et al. 2000), a large concentration of hot material must be located at low latitudes to ensure the observed veiling amplitudes (see details in Mahdavi & Kenyon 1998). Since the hot spots are located next to the magnetic poles in a classical dipole configuration, we are led to conclude that TW Hya has a highly inclined field configuration. A similar argument based on the available photometric data was previously stated by Krist et al. (2000).

The veiling at 3550 Å measured directly from the blend of low excitation potential iron lines can be used to verify the flux calibrations (Sec. 3.1). Figure 5 shows the veiling versus the Balmer continuum flux at 3550 Å (which contains negligible contribution from the photosphere). The tight correlation indicates that the veiling variations and the spectrophotometric changes in this spectral region are identical.

3.2.2. The Balmer Jump

We define the observed Balmer jump as the flux ratio across the 3640 Å discontinuity, which is the intrinsic Balmer jump of the spot energy distribution diluted by the photosphere. As can be seen in Figure 3, the flux redward of the jump is not directly accessible and relies entirely on extrapolations of the Paschen continuum towards the jump. The Paschen continuum location is defined by several spectral windows, at $\lambda > 4000$ Å, lacking emission lines or strong absorption

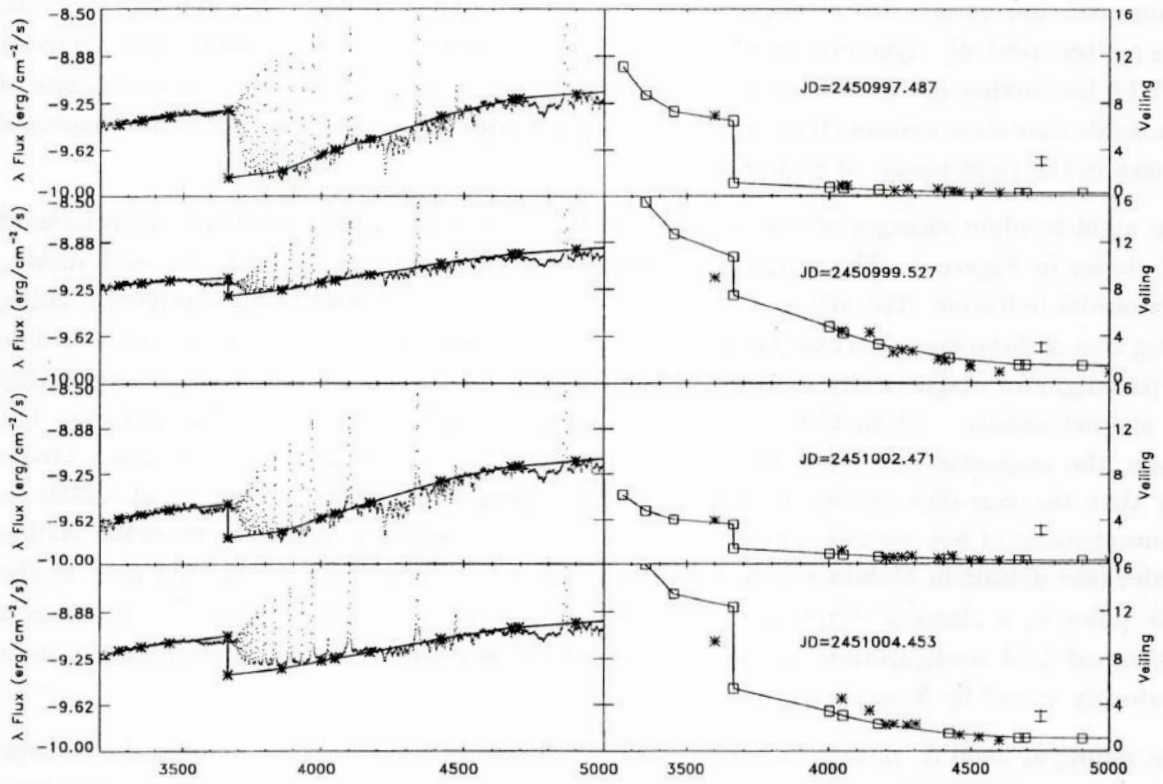

Fig. 3.— Four observations are shown on the left hand side of this figure (dots). The respective veilings are displayed on the right hand side as asterisks. Isothermal models are developed in Section 3.4 and the results (model SED and veiling) are shown as solid lined. The size of the observed Balmer jump changes severely between the first two exposures, taken two nights apart.

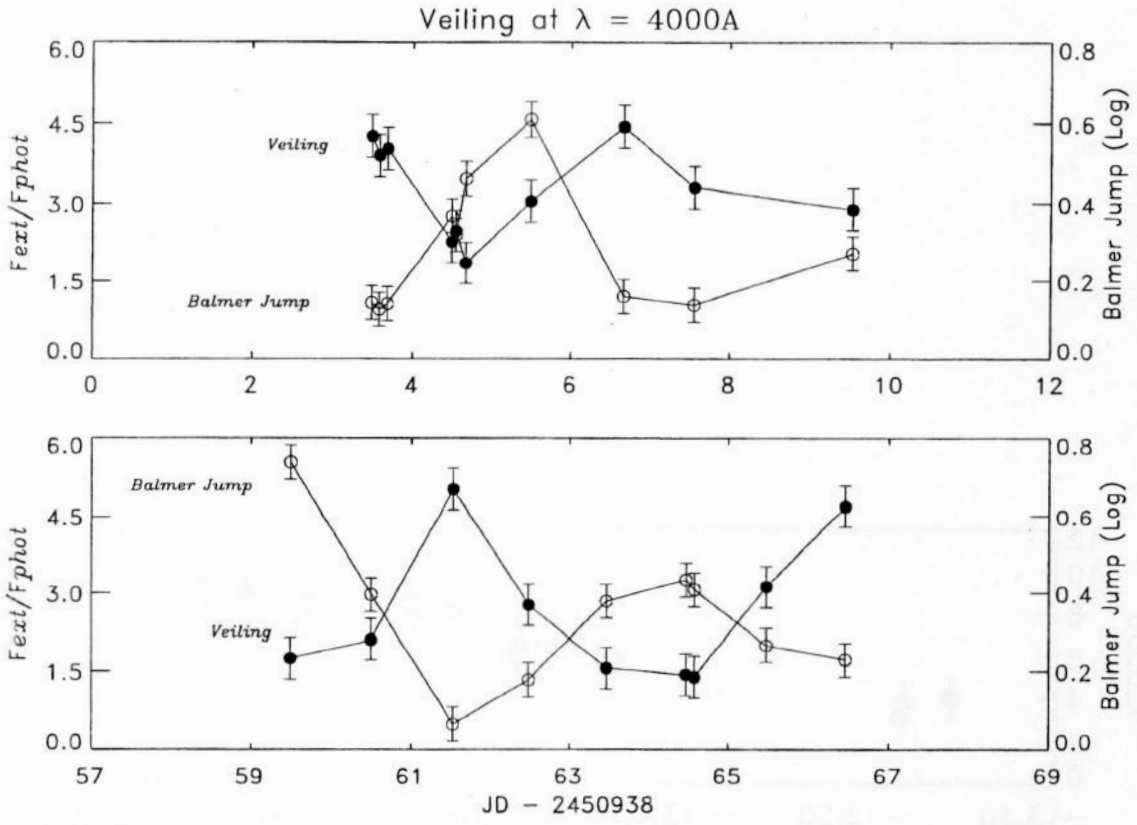

Fig. 4.— The veiling time series at 4000 Å are shown for the May and July runs (filled dots). The anticorrelation with the Balmer jump (open circles) is clearly detected.

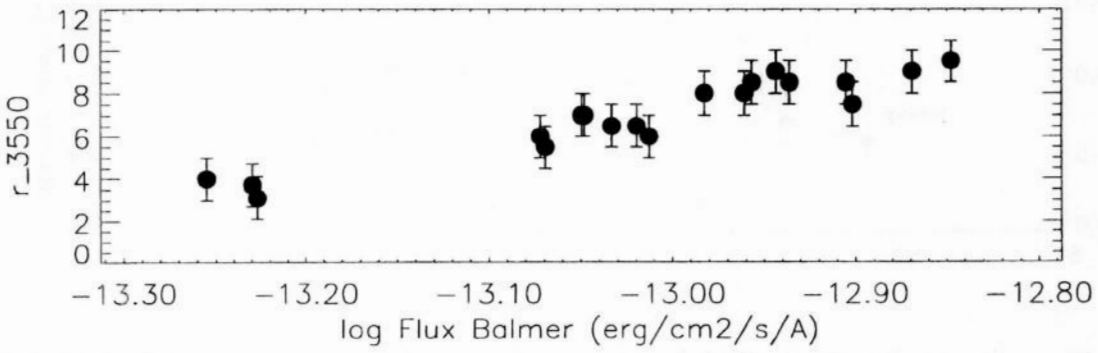

Fig. 5.— The tight correlation between the veiling at 3550 Å and the Balmer continuum fluxes verifies the flux calibrations described in Section 3.1.

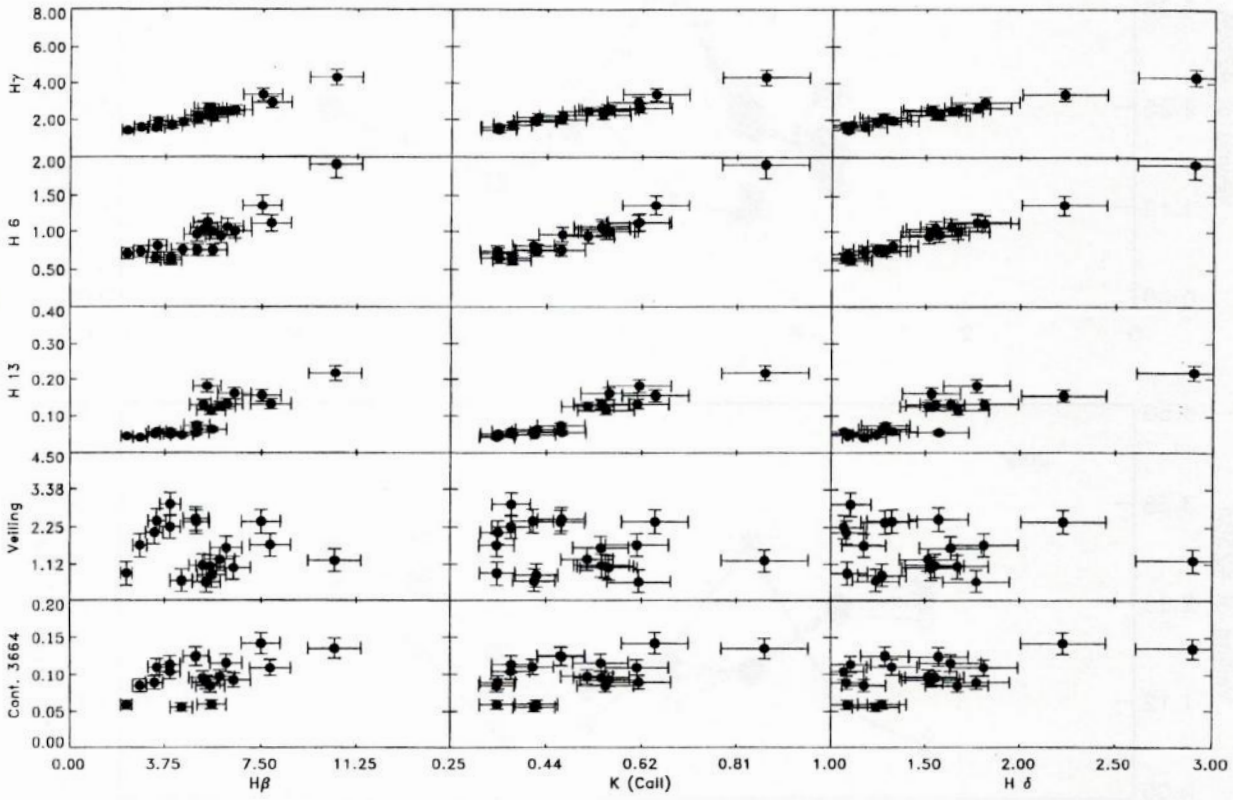

Fig. 6.— All the lines correlate with each other, indicating that they are products of a common formation mechanism (infall or wind). The line fluxes are weakly correlated with the Balmer continuum but not with the Paschen continuum veiling.

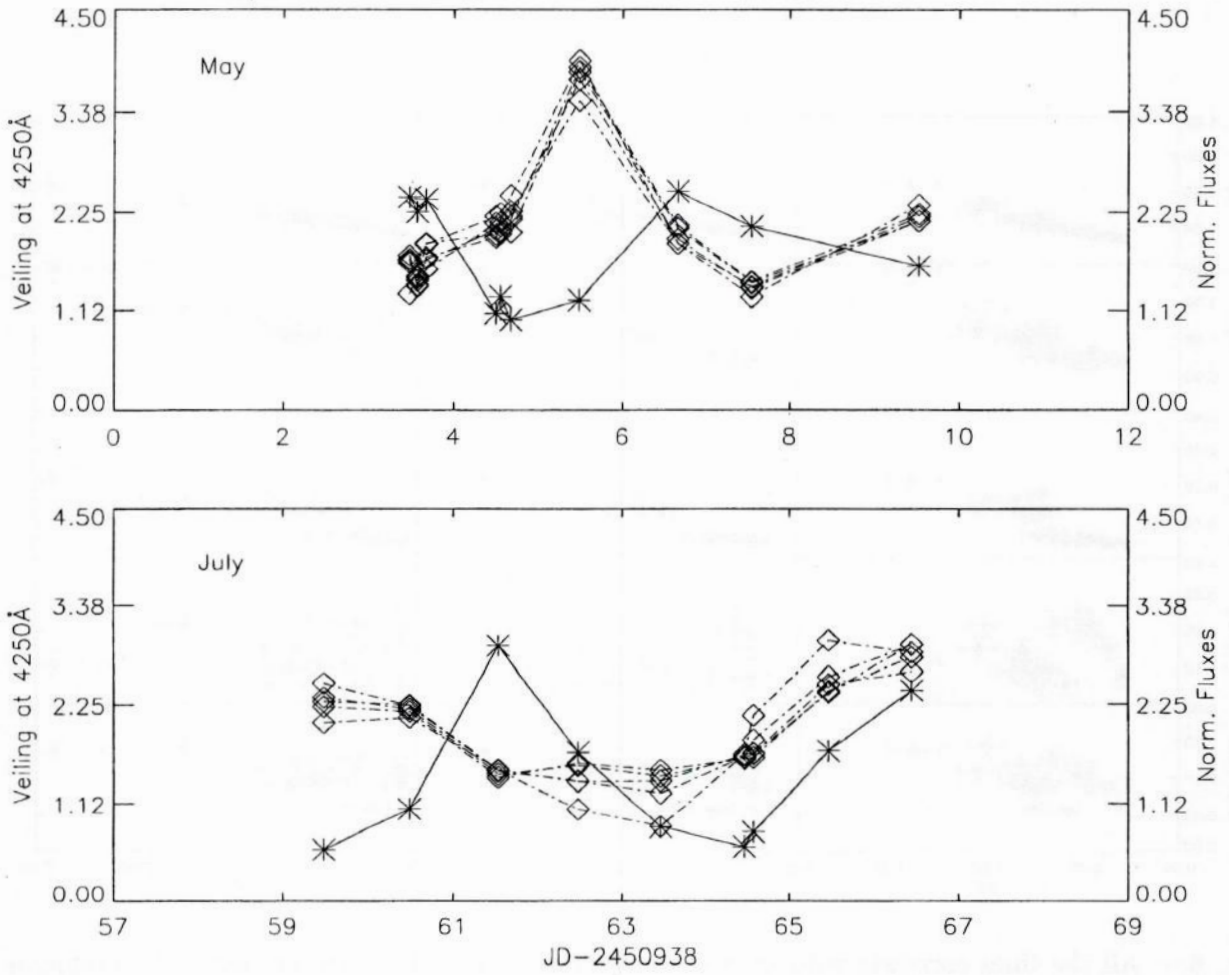

Fig. 7.— The veiling time series at 4250 Å of May and July (stars) are presented together with the time series of some of the strongest lines (diamonds), normalized to a common reference. It is apparent that the veiling and the line emission fluxes are not in phase.

features. Due to the absence of inverse PCygni absorptions and FeI / FeII emission lines in the TW Hya spectrum, the definition of such windows and the resulting extrapolation towards the Balmer jump is straightforward. For stars with mild levels of disk accretion (like GQ Lupi and TW Hya), we find that a linear fit through windows at $\lambda\lambda$ 4002, 4051, 4250, 4420, 4507, 4670 Å provides a reasonable representation of the Paschen continuum slope. This is not necessarily the case for the highly veiled T Tauri stars (like RU Lupi, EX Lupi, HO Lupi) since a forest of blended FeI - FeII emission lines artificially raises the local continuum. The linear fit through the windows is extended towards the discontinuity and defines the flux immediately redward of the jump (F_{BJ}^{red}). The blueward Balmer flux (F_{BJ}^{blue}) is measured directly from the Balmer continuum. The jump size is obtained by dividing F_{BJ}^{blue} by the flux F_{BJ}^{red}.

The resulting Balmer jump time series is displayed in Figure 4 as open circles. The jump size changes strongly from night to night and shows the same tight anti-correlation with the veiling as previously detected in GQ Lupi (VASTT1). In fact, this anti-correlation is characteristic of CTTS (see VBJ93 and CG98) and must be predicted by models.

3.2.3. The Line Emission

The flux calibration developed in Section 3.1 allows us to ascertain the line luminosities of each of the emission profiles in the format. The Balmer lines (Hβ down to H14) and the Ca II K line are well discernible in all spectra. Less conspicuous is the HeI line at 4471 Å present in all exposures. Equivalent widths and integrated fluxes are computed for all the lines and placed in Table 1. These fluxes are not corrected for the circumstellar extinction. The average veilings at $\lambda\lambda$ 3550, 4250 and 5000 Å are also displayed in Table 1.

The strong emission profiles contain distinct components probing different formation regions. Modeling and following the variable change in shape and intensity of each of these particular features constitutes the major goal of our previous paper (Alencar & Batalha 2002) and requires high resolution data (see also Johns-Krull & Basri 1997; Alencar & Basri 2000; Beristain et al. 2001). We cannot distinguish different components at our resolution. The line fluxes of Table 1 incorporate contributions from physically distinct regions. None of the profiles show features of direct or inverse PCygni profiles. We find that the line emission fluxes correlate with one another indicating how dependent they are on a common forming mechanism or gas location (Figure 6). The line fluxes are not correlated with the veiling in the Paschen continuum, but large Hβ fluxes are associated with large Balmer continuum fluxes.

The line emission time series of some of the strongest line profiles are shown in Figure 7 (squared symbols), normalized to a standard flux level. They all share a similar behavior, always strengthening or fading in phase. The veiling time series at 4250 Å is also indicated (star symbols). By inspecting Figure 7, it is readily apparent that the Paschen continuum excess (veiling) is not in phase with the line fluxes. However, as indicated in Figure 6, large Hβ fluxes are consistent with

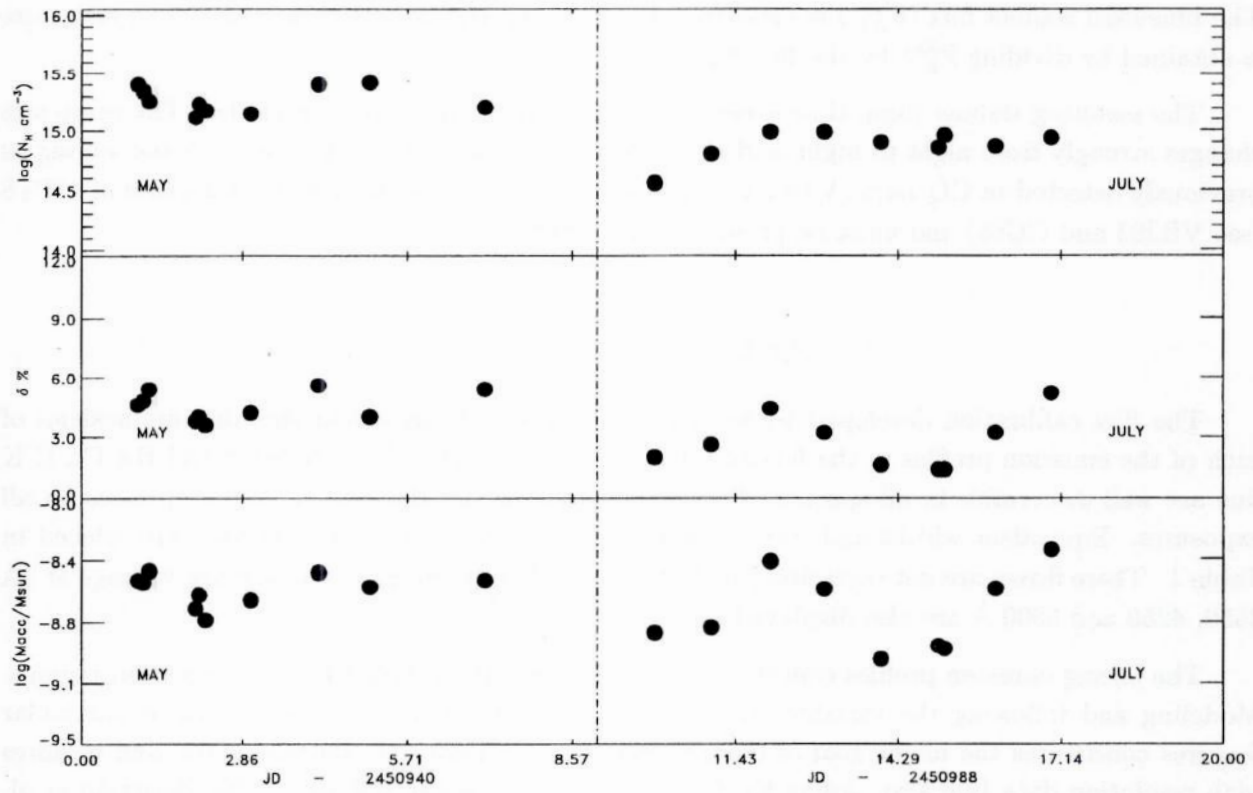

Fig. 8.— We develop model parameters of the impacted zone by assuming that the continuum emission originates in a gas of uniform temperature and density. The evolution of the dominant spot gas density, projected spot area (δ), and the mass accretion rate are displayed as a function of the Julian Date.

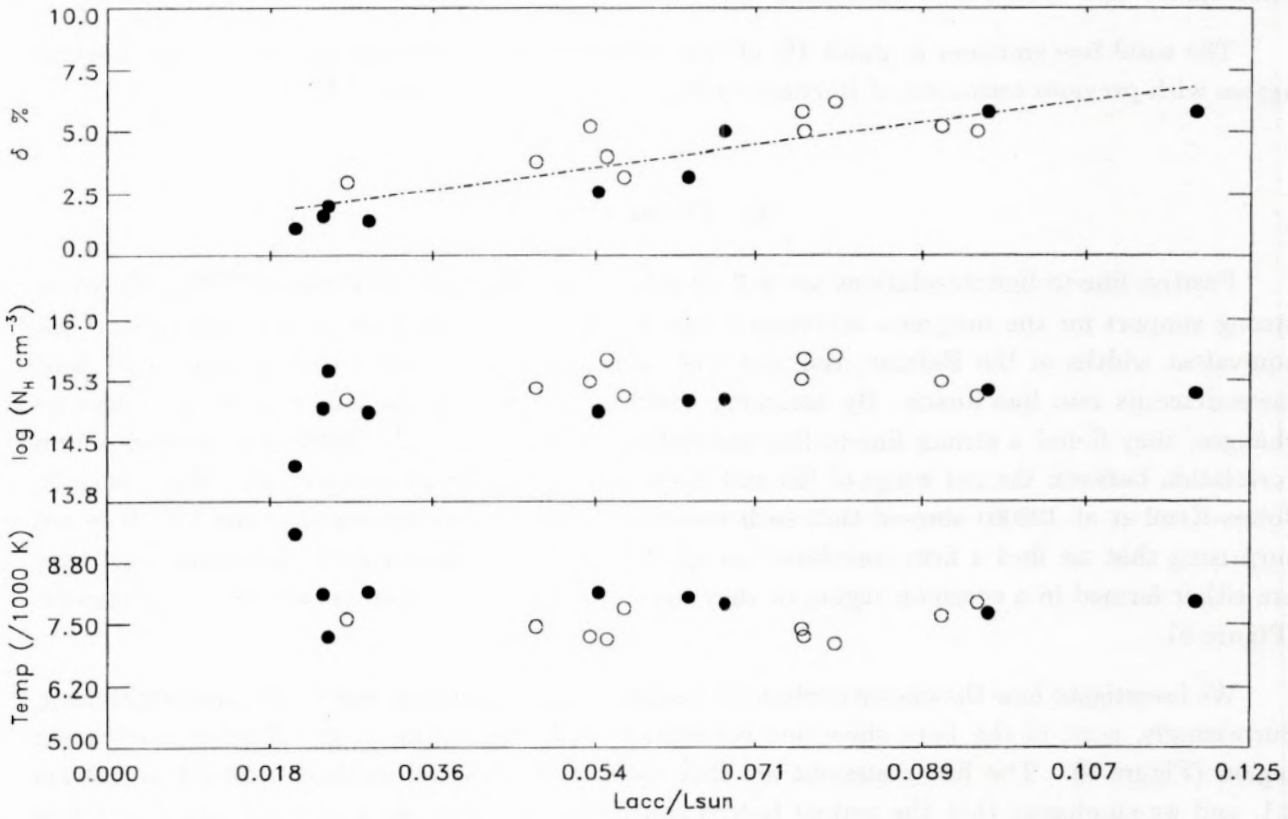

Fig. 9.— The accretion luminosity based on the model parameters are compared with the parameters themselves. May and July models are presented by open and closed circles respectively. The broken line in the upper panel indicates a linear fit to the projected area as a function of accretion luminosity.

large Balmer continuum fluxes. This crude correlation does not come as a surprise if both features are formed in the same region. The shock models (CG98) predict that the bulk of Balmer continuum originates in the accretion funnel prior to the impact, and the correlation is a confirmation of the model predictions. The slab models, on the contrary, locate the Balmer continuum emission in the photosphere below the post shock region. The continuum opacity is controlled by the local gas parameters, and the Paschen continuum is always less opaque, yielding to line formation. The correlation, then, indicates that some of the observed line emission originates in the illuminated photosphere and should be considered in efforts to explain line emission profiles in CTTS.

The total line emission is about 1% of the continuum emission throughout the season which agrees with previous estimates of Hartigan et al. (1989) for a single star (BP Tau, $\sim$ 5%).

4. Discussion

Positive line-to-line correlations are well established for a large set of classical TTS and provide strong support for the magnetic accretion scenario. Johns-Krull & Basri (1997) determined line equivalent widths of the Balmer, HeI and CaII emission lines of DF Tau and converted those measurements into line fluxes. By assuming that the veiling was the only source of continuum changes, they found a strong line-to-line correlation. Gullbring et al. (1996) also derived a firm correlation between the red wings of Hα and Hβ with the CaII broad components. More recently, Johns-Krull et al. (2000) showed that such line-to-line correlations prevailed in the UV. It is not surprising that we find a firm correlation of all the lines with one another, indicating that they are either formed in a common region or they are subject to a common enhancement mechanism (Figure 6).

We investigate how the excess continuum emission behaves in response to the line brightening. Surprisingly, none of the lines show any correlation with the veiling in the Paschen continuum region (Figure 6). The line emissions are flux calibrated with the method outlined in Section 3.1, and we emphasize that the scaling factors converting the observed fluxes into absolute fluxes depend themselves on the veiling: $(1+r_\lambda)*F_{phot}$, where r_λ is the veiling and F_{phot} is the continuum photospheric flux. The large majority of studies seeking correlations between the veiling and line emission are based on high resolution data, where the total line fluxes (Fl) are obtained from the observed line equivalent widths (EW) and the veiling: $Fl = EW\ (1 + r_\lambda)$. Therefore, our fluxes are proportional to the same scaling factor. The lack of correlation is not a problem with the adopted standard. A completely independent set of veiling distributions computed with the star Gl 825 (the K7 template in VASTT1) yields the same results.

The standard scenario of disk accretion predicts that the excess continuum emission originates next to the impacted region (CG 98), whereas the bulk of the line emission originates in the infalling gas (Muzerolle et al. 2000). Line and continuum flux excesses depend directly on the disk mass accretion rate, with the disk simultaneously providing material to boost the impact and to feed

the magnetic tubes where the lines will brighten. Thus, within the accretion scenario, line and continuum emission should brighten in phase, but the published literature indicates that this is not always the case. Basri & Batalha (1990) were the first to provide evidence that the Hα line fluxes of DR Tau and RW Aur, individually, and of a sample of 12 stars, collectively, are correlated with their veiling. Johns-Krull & Basri (1997) favor a positive correlation between the CaII line fluxes and the veiling of DF Tau, in spite of some scatter. However, the Hα line shows conflicting results with those of Basri & Batalha (1990). While a weak positive correlation is detected for the whole range of veiling ($r_\lambda < 3.5$), no correlation is detected for $r_\lambda < 2.0$, suggesting that the veiling data points larger than 2.0 drive the correlation. This explanation can also be applied to the apparent correlation between the HeI broad line component with the veiling. The Hβ line flux and the veiling are not correlated. The model veilings of Valenti et al. (1993), in agreement with the observed veilings, show a slightly positive correlation with the observed Hβ equivalent width. The correlation is enhanced if the line equivalent widths are further converted into line fluxes. No apparent correlation between the corrected Hβ equivalent widths and the veilings is found for GQ Lupi (VASTT1). Another example of positive correlation is provided by Johns-Krull et al. (2000). They show the UV line emission of a large sample of classical TTS correlates with the UV continuum, which is an extension of the optical veiling towards the UV. On the contrary, the analysis of Ardila & Basri (2000) on BP Tau indicates a complete lack of correlation between the Mg II UV line at 2800 Å with the local UV continuum. Several high resolution observations of TW Hya taken one year after our low resolution data yield veiling corrected equivalent widths of several lines that correlate with veiling (VASTT2). We are led to conclude that correlations among line fluxes and veiling are not a mandatory occurrence in CTTS. Projection effects of the accreting gas in the funnel and of the impacted region might play a crucial role in governing the continuum and line brightening.

In the following section we model the continuum emission region by uniform slabs where the SED and the Balmer jump are explained by the differences in the Balmer and Paschen continuum opacities. The slab depth is optically thin, implying that emission lines are likely to be formed and observed at given orientations. Therefore, it should be expected that some part of the line emission comes from the slab and should be added to that produced in the funnel.

4.1. Models of the UV-Reprocessed Atmosphere

The observations described above provide important constraints for modeling the photosphere that is being illuminated by the incoming X-rays of the impacted region (Lamzin et al. 1996). If it is assumed that an axisymmetric dipole field is mediating the accretion within a few stellar radii, and that the star-disk system is seen at a low inclination angle, then the impacted region should be in view at any observational phase. The observed changes of the continuum emission will be governed either by variable disk mass accretion towards the central star or by changes of the projected spot/ring size as the star rotates.

Models of the impacted region have been previously developed with homogeneous and isothermal slabs (Hartigan et al. 1991; Valenti et al. 1993; Gullbring et al. 1998, and VASTT1) or by solving the energy-momentum equations along the shock (Calvet and Gullbring, 1998 - CG98). CG98 conclude that the observed Paschen continuum originates in an optically thick gas that reprocesses the UV radiation of the impacted region, whereas optically thin gas emission from the pre and post shock regions governs the Balmer continuum slope. Their models are further employed to analyze the UV data of BP Tau (Ardila & Basri 2000) and to estimate the mass accretion rates of TW Hya (Muzerolle et al. 2000). Slab models are successful in predicting the optical veiling distribution and the anticorrelation between the Balmer jump with the veiling observed in a large sample of classical TTS. They assume that the whole hierarchy of hot spots on the stellar surface at a given time can be described by a uniform gas. The observed changes in continuum slope, Balmer jump and brightness are primarily interpreted as resulting from changes in the gas state - density and temperature - and in the projected spot size.

In this work, we describe the reprocessed gas of the TW Hya photosphere by homogeneous slabs. Briefly, the continuum excess emission is modeled by matching the veiling spectral distribution (3800 Å $< \lambda <$ 5200 Å), the Balmer and the Paschen continuum slopes, as described in VASTT1. It is assumed that the de-reddened observed flux is

$$F_{obs} = (1 - \delta)F_{phot} + \delta(F_{spot} + F_{phot}e^{-\tau_{spot}})$$

where F_{phot} is the photospheric distribution; F_{spot} and τ_{spot} are the flux and the optical depth of a spot characterized by uniform temperature and density. The parameter δ represents the integrated spot or emission ring area projected against the line of sight. We compute a grid of spot models using the CLOUDY spectral synthesis code (Ferland et al. 1998), where temperatures range from 6000 K to 16000 K and the number of hydrogen atoms is within $1.0 \times 10^{13}\,\mathrm{cm}^{-3} < N_H < 1.0 \times 10^{16}\,\mathrm{cm}^{-3}$. Filling factors of the slab range from a few tenths of a percent to 10 %. The grid steps of each model parameter are greatly reduced from those used in VASTT1, considerably expanding the number of models available to match the data. A detailed description of the model fit procedure is given in VASTT1 (section 4.4) and is summarized here. We search for a combination of gas parameters that provides optimal fits to the observed SED's (the Balmer jump and the slopes of the Balmer and the Paschen continua) and to the observed veiling distribution. The chosen model provides the smallest quadratic difference to the observed flux distribution, χ^2, defined as $10^4 \times (F_{mod} - F_{obs})^2/F_{obs}^2$.

Time series model fit parameters are displayed in Figure 8. The optical veiling growth follows rather closely the behavior of δ, the projected spot size. We illustrate the model fits for the observations at JD = 2450997.487, 2450999.527, 2451002.471 and 2451004.453 in Figure 3 (thick line). These particular observations show states of maximum and minimum veiling emission during the run and include data of the smallest and the largest Balmer jump sizes. The size of the observed Balmer jump depends essentially on how strongly the photosphere dilutes the accretion signature (towards small δ) and on the spot opacity in the vicinity of the jump. The recombination rates to level n=3 are larger than those to level n=2. Thus, as the gas density increases, the Paschen emission brightens more rapidly than the Balmer emission, thereby diminishing the jump.

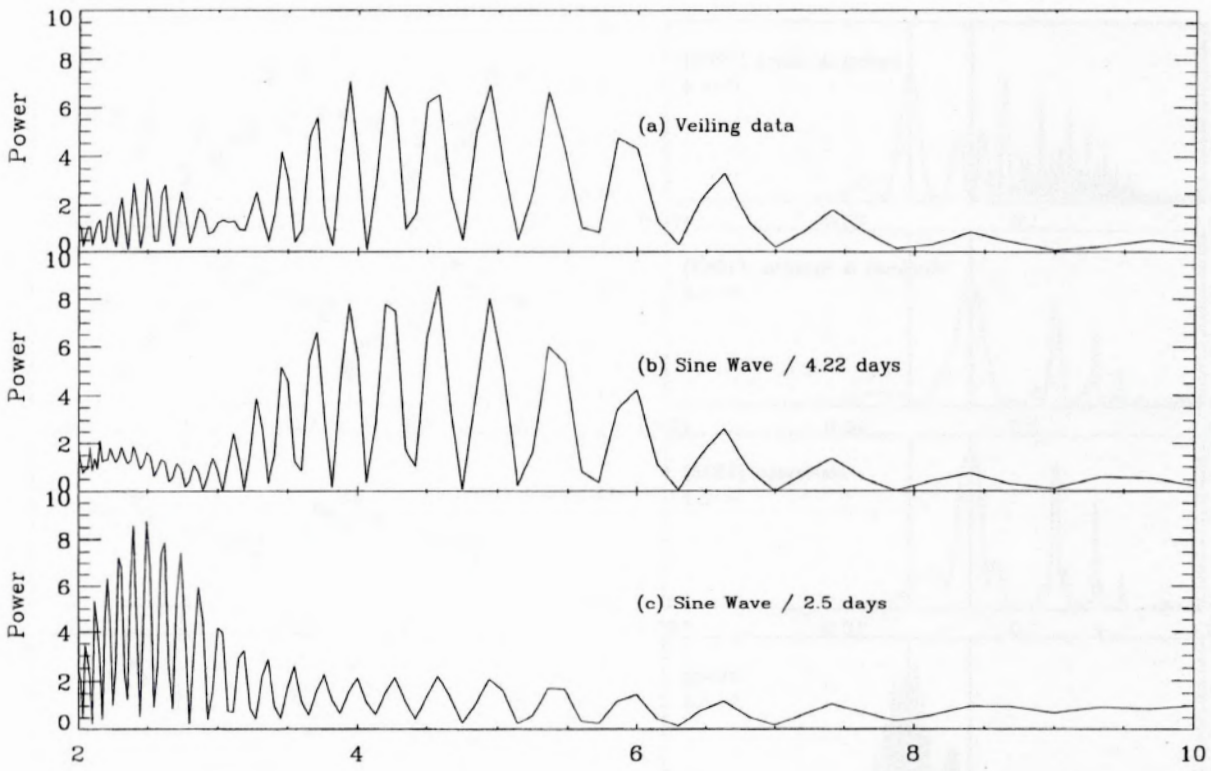

Fig. 10.— The power spectrum of the veiling time series presents two clusters of energy centered at 4.2 days and 2.5 days (a). Spectral leakage produces the ringing at these two frequencies, which is also shown in the power spectrum of pure sinusoids oscillating at approximately 4.2 day (b) and 2.5 day (c) respectively.

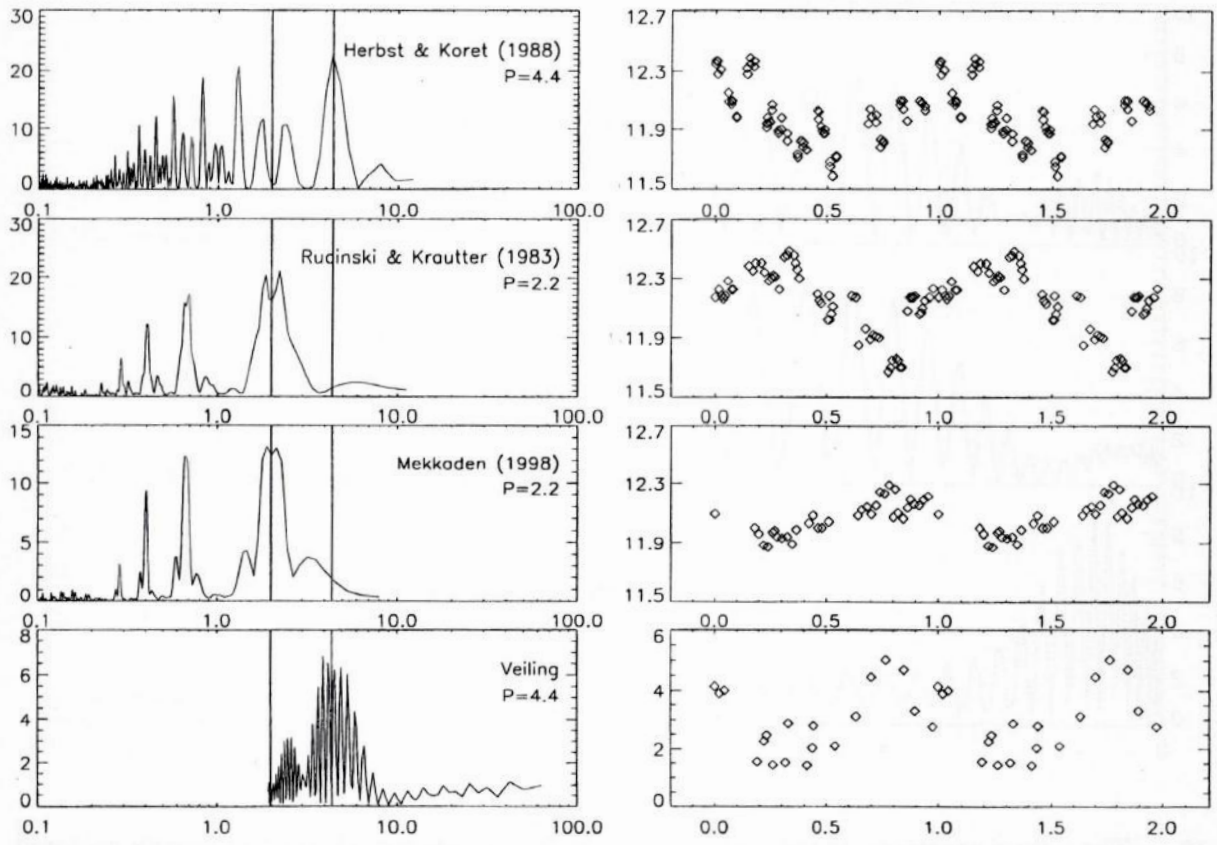

Fig. 11.— We analyze B-band observations of TW Hya using a Lomb-Scargle algorithm. Photometric data are of at least 8 consecutive nights and are taken from: **(a)** Herbst & Koret (1988); **(b)**, Rucinski & Krautter (1983); **(c)**, Mekkaden (1998); The veiling at 4225 Å is showed at **(d)**.

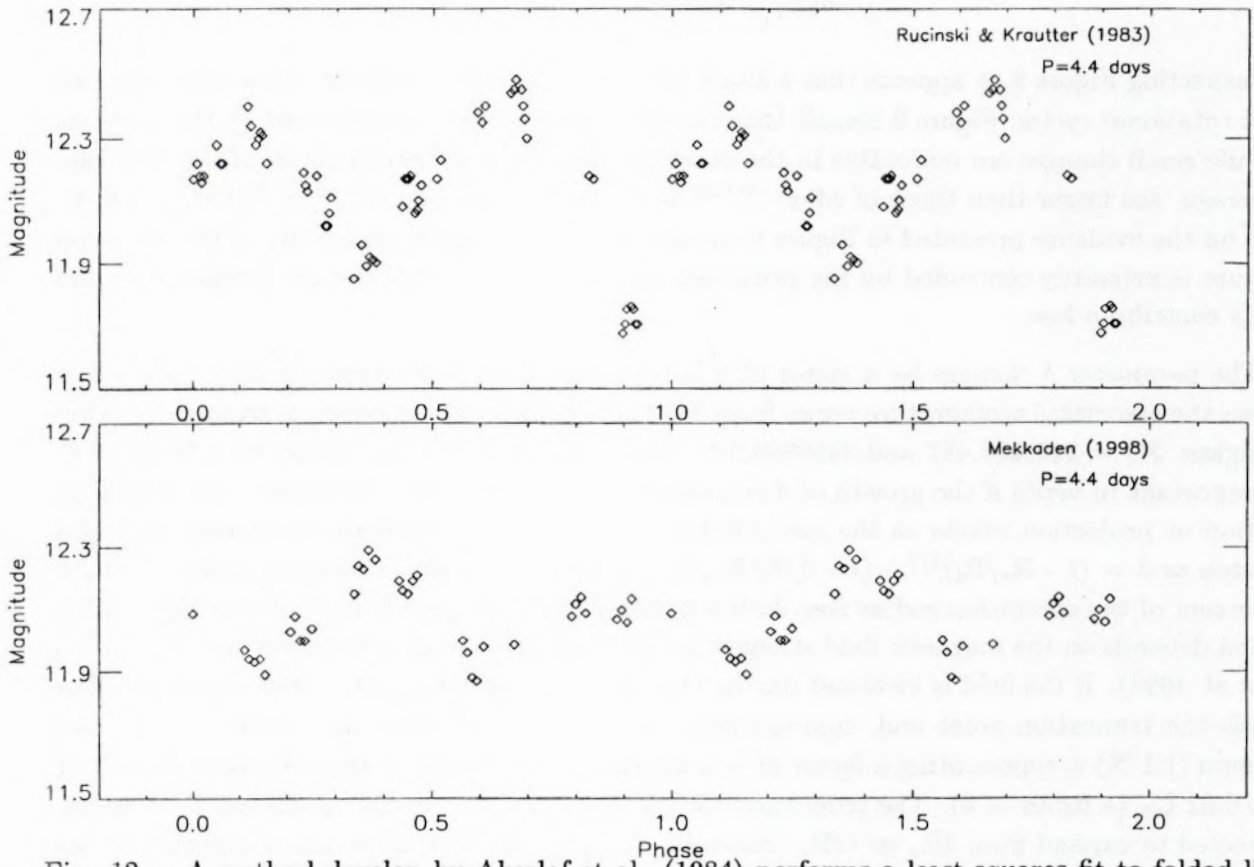

Fig. 12.— A method develop by Akerlof et al. (1984) performs a least-squares fit to folded light curves using a sum of cubic splines. The RK83 and Mekkaden (1998) photometries are folded at 4.4 days.

The dependency of the model parameters on the spot luminosity, L_{acc}, is shown in Figure 9. It is apparent that the spot size is the only parameter sensitive to the spot luminosity changes. The gas density - in number of hydrogens per cm^{-3} - and the temperature (K) fluctuate throughout the series and are strongly anticorrelated. Density and temperature control the shape of the SED with the former controlling the size of the jump. The relative growth of the projected area (δ) reflects the veiling increase in response to the mass transfer to the star:

$$\delta(\%) = 49.42\, L_{acc} + 0.9$$

Inspecting Figure 9, it appears that a single set of parameters describes the gas state over one or two rotational cycles. Figure 9 reveals that the variability is primarily governed by the spot size (δ) while small changes are noticeable in the other parameters. The temperatures of the July run, on average, are larger than those of May: $T^{July} = 8121K \pm 660K$ and $T^{May} = 7446K \pm 292$ K. Based on the evidence presented in Figure 9, we argue that the nightly variability of the accretion signature is primarily controlled by the projected size of the spot, while the gas temperature and density contribute less.

The parameter δ changes by a factor of 5 between minimum and maximum spot luminosity, whereas the associated temperature varies from 9332 K to 8128 K. These extremes happened within two nights: JD = 2450997.487 and 2450999.527, while the parameter L_{acc} grows by a factor of 6. It is important to verify if the growth of δ represents either short term variations of the disk mass accretion or projection effects as the star rotates. Current model predictions estimate the total spot area as $\delta = (1 - R_\star/R_t)^{1/2} - (1 - 3/2 \times R_\star/R_t)^{1/2}$ where R_t is the truncation radius within a few percent of the corotation radius (see Ardila & Basri 2000; see also Ostriker & Shu 1995). This location depends on the magnetic field strength ($\propto B^{4/7}$) and on the disk accretion rate ($\propto \dot{M}_D^{-2/7}$, Shu et al. 1994). If the field is invariant during the cyclic change of L_{acc}, then disk accretion alone controls the truncation point and, consequently, the spot size. Between maximum (5.6 %) and minimum (1.1 %) δ, representing a factor of 5 in apparent size, the spot luminosity fades from 0.12 $L_\odot$ to 0.02 $L_\odot$ (a factor of 6). The truncation radius (R_t), according to the expression for δ above, is expected to expand from $4R_\star$ to $12R_\star$. Since $R_t \propto \dot{M}_D^{-2/7}$, the disk accretion is expected to fall by a factor of 70 (if B is kept constant), not 6.0 as we measure from the observed veiling. We are therefore compelled to suggest that projection effects dominate the changes.

4.2. Mass Accretion

The total spot luminosity sets a lower limit to the disk mass accretion. Part of the accretion energy is radiated away by lines in the funnel and impacted region, and part is lost in winds. It is possible to establish a lower limit to the accretion luminosity by integrating the spot emission over the entire wavelength range. This approach has the virtue of being entirely model free and relies on how well the extrapolation of the external emission is done towards the ultraviolet. This

approach is taken in Alencar & Batalha (2002) who combine the high and the (not simultaneous) low resolution veiling distribution to infer the excess emission over the whole optical range. The archival IUE data is used as a reference at very short wavelengths.

Model parameters can also be used to determine the spot luminosity. As can be seen in Figure 3 the model SED matches the observations and fits the veiling distribution. Thus, $L_{acc} = \delta 4\pi R_\star^2 \int F_\lambda^{ext} d\lambda$, where δ and F_λ^{ext} are model dependent (see Figure 9). The model $\int F_\lambda^{ext} d\lambda$ is, in general, less than σT^4 for a slab of a given temperature, T, since the Paschen continuum is optically thin and becomes more opaque as the gas density grows in response to the mass accretion.

The accretion, or spot, luminosities provide a rough estimate to the mass accretion rate if $L_{acc} = GM\dot{M}_{acc}/R_\star(1 - R_\star/R_t)$. Assuming an average truncation at $5R_\star$ (Meyer et al. 1997), and adopting the stellar parameters of Table 2, the stellar accretion rates range within $1.0 \times 10^{-9}\, M_\odot yr^{-1} < \dot{M}_{acc} < 4.8 \times 10^{-9}\, M_\odot yr^{-1}$.

Our mass accretion rates are less than that estimated by Wilner et al. (2000): $\sim 10^{-8}\, M_\odot yr^{-1}$. Those authors model the gaseous disk surrounding TW Hya using VLA observations. On the other hand, our value is larger than that of Muzerolle et al. (2000) who estimated $\dot{M}_{acc}$ of $\sim 4 \times 10^{-10}\, M_\odot$ yr^{-1} consistent with $L_{acc}/L_\odot = 0.012$. The empirical calibration of Gullbring et al. (1998) allows an estimation of the $L_{acc}/L_\odot$ with a simple relation:

$$\log(L_{acc}/L_\odot) = 1.09^{0.04}_{-0.18} \log(L_U/L_\odot) + 0.98^{0.02}_{-0.07}$$

where L_U is the unreddened luminosity of the U band after subtracting the flux emission of the underlying photosphere. We take the averaged U - band photometry of Rucinski & Krautter (1983), de-reddened ($A_V = 0.1$) and integrated over the band pass ($\int U_\lambda F_\lambda^{ext} d\lambda$). The resulting luminosity, $\log(L_U/L_\odot) = -2.035$, is introduced in the right hand side of the above relation, yielding $L_{acc}/L_\odot$ $= 0.058$, which is a factor of 5.0 larger than that of Muzerolle et al. (2000) but well within our range. The accretion luminosity would decrease to 0.05 for $A_V = 0.0$. It is possible that variability alone (disk or magnetosphere) can be invoked to explain the apparent discrepancy of the accretion luminosities predicted by Muzerolle et al. (2000) and us.

4.3. Periodogram Analysis

One of the major goals of time series programs such as VASTT is to test the magnetic accretion scenario whereby magnetic tubes control the gas accretion near the star. A corotating magnetosphere will presumably modulate spectral features in the wings of emission lines (see Johns & Basri 1995) as well as broad band magnitudes, with periods reflecting that of the stellar rotation. Therefore, in spite of out modest sampling rate, we investigate if periodic behavior is present in our veiling or line emission time series. We perform a Fourier analysis, specific to unevenly sampled data – the Lomb-Scargle periodogram (Gilliland & Baliunas 1987).

False-alarm probabilities are computed via Monte Carlo simulation to determine the number of independent frequencies tested for each time series. A large number ($\sim$ 300) of Gaussian noise vectors are generated for each time series and their Lomb periodograms are computed. The maximum amplitude of each periodogram is noted, resulting in a vector, z, of 300 such values for each time series. The cumulative distribution function (CDF) of each vector is computed, and a false-alarm function of the form $1-(1-e^{-a})^N$ is fit to the CDF (minimizing the chi-squared statistic). Here, a is a vector sampling the range of periodogram peaks found in z, and N, the free parameter, is the number of independent frequencies. The best fit to the CDF yields an estimate of the number of independent frequencies examined for a given time series. Finally, the false-alarm probability associated with a given periodogram peak is computed as $FAP = 1-(1-e^{-amp})^N$, where amp is the amplitude of the peak and N is the number of independent frequencies. These estimates are valid only under the assumption that the noise is normally distributed, and should, therefore, be considered as lower estimates.

The best spectral region for analysis of the veiling variability is 4250 Å, corresponding to the rising part of the veiling distribution probed by numerous absorption lines (especially the CaI line at 4226 Å). The power spectrum is presented in Figure 10a. It shows two clusters of energy centered at approximately 4.2 and 2.5 days. The ringing at these frequencies is due to spectral leakage as shown in the power spectrum of pure sinusoids oscillating at the respective frequencies (Figure 10b,c). The 4.2 day signal shows the largest energy, resulting in a false-alarm probability of 0.06.

Examples of broad-band time series analysis of this object at different epochs exist in the literature. Herbst & Koret (1988, HK88) find a 4.5 day and 1.28 day period in their 1988 BVR photometry. The authors also analyze the Rucinski & Krautter (1983, RK83) UBVRI photometry, recovering solutions at 2.25 and 1.83 days. They note that the 4.5 day timescale is the beat period of the 1.28 day timescale with the diurnal cycle. This is also true of the 2.25 day and 1.28 day periods: a 1.28 day periodicity will beat with the diurnal cycle every 2.25 days. Consequently, Herbst & Koret (1988) question the reliability of the longer timescales as truly stellar phenomena. More recently, Mekkaden (1998) derived a 2.196 day solution, consistent with the 2.25 day period of RK83. None of the proposed periods are detected in the Hipparcos photometry which is sparsely distributed over 5 years (see Kastner et al. 1999 for details).

We collect all of the archival photometric data and analyze the B-band observations using algorithms which employ sinusoids (Lomb-Scargle periodogram) and other algorithms which employ cubic splines as their basis functions. The latter method, developed by Akerlof et al. (1984), performs a least-squares fit to folded light curves using a sum of cubic splines. In this manner, non-sinusoidal variability can be identified. Figure 11 shows the Lomb-Scargle periodogram for each data set. Maximum energy falls at either the 4.4-day timescale (the HK88 photometry and the veiling time series) or one half of this value (RK83 and Mekkaden photometry). The latter data sets yield double-peaked light curves when folded at the 4.4-day timescale. Allowing for non-sinusoidal variability, the cubic B-spline algorithm of Akerlof et al. yields a minimum chi-square solution for all data sets of 4.4 days. The RK83 and Mekkaden photometry folded to the Akerlof

solutions are shown in Figure 12.

The line flux time series presented in Figure 7 indicates quasi-cyclic behavior in both epochs of observations. Our periodogram analysis yields a cluster of solutions centered at 5.5 ± 0.5 days for all lines. Spectral leakage is severe due to the poor time sampling and short data record as was the case for the veiling data. The TW Hya high resolution campaign carried out in 1999 and 2000 (VASTT2) does not reproduce this solution for the lines but shows, instead, a 2.9 day period in one of the runs. Given the modest time sampling of our campaigns, we are unable to support either solution. However, we can conclude that there is not a strong rotational signature dominating the line flux variations. Models of line formation in an accreting funnel usually invoke rigid field line configurations as well as constant accretion rates in order to make the problem treatable (Muzerolle et al. 2000). Within this framework, line profile variations should beat with the stellar spin (see Johns & Basri 1995). However, our data do not support this prediction. The observations suggest there is an additional mechanism operating which is responsible for the line flux variations. We note that quasi-cyclic changes in stellar accretion rate or in the emitting volume might lead to fluctuations in line features that are independent of the stellar rotation.

4.3.1. The Spot Latitude

Within the magnetic dipole field scenario, let's assume that a large parcel of the accreting gas is directed to a single and dominant spot/ring structure. Since L_{acc} is changing in a daily basis, we are lead to conclude that the dipole field is inclined with respect to the axis of rotation. Furthermore, Potter (2001) sets an upper limit of 15° for the disk/star inclination angle which can be used to determine the spot latitude. The maximum spot luminosity occurs when the geometric rotational axis and the spot baricenter are coplanar with the line of sight, and the rotational axis is not in between these two points. The geometric pole is in between the line of sight and the spot during minimum light. Thus, $L_{acc}^{max}/L_{acc}^{min} \sim \cos(\beta - i)/\cos(\beta + i)$, where β and i are the spot colatitude and inclination angle respectively (see Mahdavi & Kenyon 1998). The ratio between maximum and minimum spot brightness is of the order of 6.0, implying that β has to be larger than $\sim 70°$.

5. Conclusions

We present 19 low resolution observations of TW Hya, a classical T Tauri star in one of the closest associations. The observed spectral format lies within the range 3100 Å$< \lambda <$ 5100 Å where the optical veiling peaks, is heavily populated by emission lines and includes the Balmer jump. The occurrence of several lines together with a well determined continuum excess distribution yields studies of line and continuum emission.

The veiling distribution of each exposure is measured and subtracted from the flux calibrated

spectrum, revealing the energy distribution of the TW Hya photosphere. Seven exposures taken under good weather condition yield a bona fide photosphere of TW Hya. The latter can be easily accessed by reading the star BD+63^o 013 from the Jacoby, Hunter & Christian (1984) library and applying the factor 0.095 on the distribution. The stellar photosphere is dimmer than previously established, indicating that TW Hya is nearly 30 Myr old and has a gravity of $\log g = 4.5$ (Figure 2).

The Balmer jump size and the veiling adjacent to the jump are strongly anticorrelated (Figure 4), a behavior similar to that of GQ Lupi, another mildly accreting CTTS (VASTT1). The amplitude of the veiling variations during the May and July observations has the same size and ranges within $1.5 < r_{4250} < 4.0$ on time scales of about 2.5 days. It has a cyclic behavior (Figure 4). If a magnetic dipolar field is truncating the disk and governing the accretion near the star vicinity, it is necessarily inclined with respect to the axis of rotation, or else no continuum variability would be detected.

The veiling does not correlate with the line fluxes (Figure 6 and Figure 7) and all the lines correlate with one another throughout the series. We show that the dominant source of the UV and optical veiling variations is the change in the projected size of the spot/ring structure as the star rotates (Figure 9). The measured line emission fluxes are also subjected to projection effects. We conclude that the positive line-to-line correlation indicates a common origin for the bulk of the line emission, probably in the accreting funnel. However, the spot and funnel projections of a particular CTTS might not necessarily grow in phase, yielding the apparent lack of correlation between the continuum and line emission excesses we measure. High resolution observations of TW Hya done two years later, show a positive correlation between line emission components and veiling (VASTT2).

The atmosphere of TW Hya must contain surface features that are common to all magnetically active young stars, in particular, dark spots. In fact, the light curve of weak TTS's are governed by cool spots that cross the line of sight as the star spins (Herbst et al. 1994). In our attempt to model the continuum emitting region, we assume that the photometric variability of TW Hya is solely governed by a distribution of hot spots characterized by uniform temperatures and densities. We show that the projected spot size grows from 1.0 to 5.0 % of total stellar surface. The spot luminosity grows by a factor of 10 within the range $0.01 < L_{acc}/L_{\odot} < 0.1$ (Figure 9). Assuming an average truncation radius at $5R_{\star}$ we estimate a mass accretion rate range within $1.0 \times 10^{-9}\,M_{\odot}yr^{-1} < \dot{M}_{acc} < 4.8 \times 10^{-9}\,M_{\odot}yr^{-1}$.

The nightly change of the spot projected size allows to infer the spot latitude. Based on the current estimations of the star-disk system inclination ($< 15°$, Potter 2001) the ratio between maximum and minimum continuum veiling emission indicates that spot latitude is less than 20° away from the stellar equator.

We perform a periodogram analysis on the veiling time series and on previously published photometry. We conclude that a 4.4 day period solution is common to both data sets and propose this value as the true rotation period of TW Hya. The stellar radius of TW Hya (Table 2) and its

rotational period of 4.4 days indicate an equatorial velocity of about 9 Km/s. The projected value will be less and depends on the system inclination angle.

This research is based on data collected on the ESO 1.52m telescope at La Silla, partly run by the Observatório Nacional-CNPq as a results of the Brazilian-ESO agreement. S.H.P.A. acknowledges support from FAPESP (grant 00/06244-9). We thank our anonymous referee for insightful comments on the manuscript.

REFERENCES

Alencar, S.H.P., & Basri, G. 2000, AJ, 119, 1881

Alencar, S.H.P., & Batalha, C. 2002, ApJ, 571, 378 - VASTT2

Ardila, D. R., & Basri, G. 2000, ApJ, 539, 834

Baraffe,I, Chabrier,G., Allard,F., & Hauschildt,P.H. 1998, A&A, 337, 403

Basri, G., & Batalha, C.C. 1990, ApJ, 363, 654

Batalha,C., & Batalha, N.M. 2001, *ASP Conf. Ser.* vol 244, 135

Batalha, C., Lopes, D.F., Batalha, N.M. 2001, ApJ, 548, 377 - VASTT1

Beristain, G., Edwards, S., Kwan, J. 2001, ApJ, 551, 1037

Blondel,P.F.C., Talavera, A., Djie, H.R.E.T.A. 1993, A&A, 268, 624

Brandner,W., Zinnecker,H., Alcalá,J.M., Allard,F., Covino,E., Frink,S., K'ohler,R., Kunkel,M., Moneti,A., & Schweitzer, A. 2000, AJ, 120, 950

Budding,E. 1993, Cambridge University Press, ISBN 0-521-41867-4

Calvet, N. & Gullbring, E. 1998, ApJ, 509, 802 - CG98

Cardelli,J.A., Clayton,G.C., & MathisJ.S. 1989, ApJ, 345, 245

Costa,V.M., Lago,M.T.V.T., Norci,L., & Meurs,E.J.A. 2000, A&A, 354, 621

Covino, E., Terranegra, L., Franchini, M., Chavarria-K., C., & Stalio, R. 1992, A&AS, 94, 273

de la Reza, R., Torres, C.A.O., Quast, G., Castilho, B.V., & Vieira, G.L. 1989, ApJ, 343, L61

Ferland, G.J., Korista,K.T., Verner,D.A., Ferguson,J.W., Kingdon,J.B., & Verner, E.M. 1998, PASP, 110, 761

Franchini,M., Covino,E., Stalio,R., Terranegra,L., & Chavarria-K., C. 1992, A&A, 256, 525

Gregorio-Hetem, J., Lepine, J.R.D., Quast, G.R., Torresr, C.A.O., & de la Reza, R. 1992, AJ, 103, 549

Gullbring, E., Petrov, P.P., Ilyin, I., Tuominen, I., Gahm, G.F., & Lodén, K. 1996, A&A, 314, 835

Gullbring, E., Hartmann L., Briceno C., & Calvet N. 1998, ApJ, 492, 323

Hartigan,P., Hartmann,L., Kenyon,S. ,Hewett,R., & Stauffer,J. 1989, ApJS, 70, 899

Hartigan,P., Kenyon,S.J., Hartmann,L., Strom,S.E., Edwards,S., Welty,A.D., & Stauffer,J. 1991, ApJ, 382, 617

Hartmann,L., Hewett,R., & Calvet,N. 1994, ApJ, 426, 669

Herbig,G.H., & Bell,K.R. 1988, Lick Observatory Bulletin, Santa Cruz: Lick Observatory.

Herbst, W.& Koret,D.L., 1988, AJ, 96, 1949

Herbst,W., Herbst,D. K., Grossman,E. J., & Weinstein,D. 1994, AJ, 108, 1906

Jacoby,G.H., Hunter,D.A., & Christian, C.A. 1984, ApJS, 56, 257

Johns,C.M., & Basri, G. 1995, ApJ, 449, 341

Johns–Krull,C.M., & Basri, G. 1997, ApJ, 474, 433

Johns–Krull,C.M., Valenti,J.A., & Linsky,J.L. 2000, ApJ, 539, 815

Johnson,H. 1966, ARA&A, 18, 439

Kastner,J.H., Zuckerman, B., Weintraub, D. A., & Forveille, T. 1997, Science, 277, 67

Kastner,J.H., Huenemoerder,D.P., Schulz,N.S., & Weintraub, D.A. 1999, ApJ, 525, 837

Königl,A. 1991, ApJ, 370, L39

Krist,J.E., Stapelfeldt,K.R., Menard,F., Padgett, D.L., & Burrows, C.J. 2000, ApJ, 538, 793

Lamzin,S.A., Bisnovatyi-Kogan,G.S., Errico,E., Giovannelli,F., Katysheva,N.A., Rossi,C., & Vittone,A.A. 1996, å306, 877

Mahdavi,A., & Kenyon,S.J. 1998, ApJ, 497, 342

Mekkaden,M.V. 1998, A&A, 340, 135

Meyer,M.R., Calvet,N., & Hillenbrand,L.A. 1997, AJ, 114, 288

Montes,D., & Martin,E.L. 1998, A&A, 128, 485

Muzerolle,J., Calvet,N., Briceno,C., Hartmann,L., & Hillenbrand,L.A. 2000, ApJ, 535, L47

Ostriker,E.C., & Shu,F.H. 1995, ApJ, 455, L155

Rucinski, S.M., Krautter, J. 1983, A&A, 121, 217

Rucinski,S.M. 1988, Informational Bulletin on Variable Stars, 3146, 1

Shu,F.H., Najita,J., Ostriker,E.C., Wilkin,F., Ruden,S., & Lizano,S. 1994, ApJ, 429, 781

Sterzik,M.F., Alcalá,J.M, Covino,E., & Petr, M.G. 1999, A&A, 346, L41

Strom,S.E., Edwards,S., & Skrutskie,M. F. 1993, in Protostars and Planets III, University of Arizona Press, ISBN:0816513341, p. 837-866.

Valenti,J.A., Basri,G., & Johns,C.M. 1993, AJ, 106, 2024

Webb,R.A., Zuckerman,B., Platais,I., Patience,J., White,R.J., Schwartz,M.J., & McCarthy,C. 1999, ApJ, 512, L63

Weintraub,D.A., Kastner,J.H., & Bary,J.S. 2000, ApJ, 541, 767

Wichmann,R., Bastian,U., Krautter,J., Jankovics,I., & Rucinski, S.M. 1998, MNRAS, 301, L39

Wilner,D.J., Ho,P.T.P., Kastner,J.H., & Rodriguez, L.F. 2000, ApJ, 534, L101

Zuckerman,B., Webb,R.A., Schwartz,M., & Becklin,E.E. 2001, ApJ, 549, L233